Survey of gravitational wave memory in intermediate mass ratio binaries

Tousif Islam,[1,2,3,4,*] Scott E. Field,[2,3] Gaurav Khanna,[1,3,5] and Niels Warburton[6]

[1]*Department of Physics, University of Massachusetts, Dartmouth, Massachusetts 02747, USA*
[2]*Department of Mathematics, University of Massachusetts, Dartmouth, Massachusetts 02747, USA*
[3]*Center for Scientific Computing and Visualization Research, University of Massachusetts, Dartmouth, Massachusetts 02747, USA*
[4]*Kavli Institute for Theoretical Physics, University of California, Santa Barbara, California 93106, USA*
[5]*Department of Physics, University of Rhode Island, Kingston, Rhode Island 02881, USA*
[6]*School of Mathematics and Statistics, University College Dublin, Belfield, Dublin 4, Ireland*

(Received 22 September 2021; accepted 23 June 2023; published 20 July 2023)

The nonlinear gravitational wave (GW) memory effect is a distinct prediction in general relativity. While the effect has been well studied for comparable mass binaries, it has mostly been overlooked for intermediate mass ratio inspirals (IMRIs). We offer a comprehensive analysis of the phenomenology and detectability of memory effects, including contributions from subdominant harmonic modes, in heavy IMRIs consisting of a stellar mass black hole and an intermediate mass black hole. When formed through hierarchical mergers, for example when a GW190521-like remnant captures a stellar mass black hole, IMRI systems have a large total mass, large spin on the primary, and possibly residual eccentricity; features that potentially raise the prospect for memory detection. We compute both the displacement and spin nonlinear GW memory from the $m \neq 0$ gravitational waveforms computed within a black hole perturbation theory framework that is partially calibrated to numerical relativity waveforms. We probe the dependence of memory effects on mass ratio, spin, and eccentricity and consider the detectability of a memory signal from IMRIs using current and future GW detectors. We find that (i) while eccentricity introduces additional features in both displacement and spin memory, it does not appreciatively change the prospects of detectability, (ii) including higher modes into the memory computation can increase signal-to-noise (SNR) values by about 7% in some cases, (iii) the SNR from displacement memory dramatically increases as the spin approaches large, positive values, and (iv) spin memory from heavy IMRIs would, however, be difficult to detect with future generation detectors even from highly spinning systems. Our results suggest that hierarchical binary black hole mergers may be a promising source for detecting memory and could favorably impact memory forecasts.

DOI: 10.1103/PhysRevD.108.024046

I. INTRODUCTION

Detection of gravitational waves (GWs) from the coalescence of binary compact objects [1,2], mostly binary black-holes (BBH), not only helps to shape our understanding about compact objects in the universe, they also provide an unique opportunity to test the predictions of the general relativity (GR) [3]. One important prediction of GR is the existence of gravitational wave memory, a permanent distortion of an idealized GW detector after the wave has passed by [4–7]. Detection of GW memory would further bolster the validity of GR, while signatures of GW memory in alternative theories of GR are expected to deviate from GR predictions [8]. Memory effects, therefore, offer a unique way to probe the nature of gravity [9].

GW memory effects could be of different types having distinct origins. Earlier studies have primarily focused on *displacement memory*, which is a lasting change on the gravitational wave strain. *Spin memory* [10] is sourced from the fluxes of the angular momentum of the binary while *center-of-mass memory* [11] effect is related to changes in the center-of-mass part of the angular momentum. For typical astrophysical sources, displacement memory is expected to be the dominant effect followed by spin memory and center-of-mass memory [11].

The displacement memory effect is the most well studied flavor of memory. Calculation of the displacement memory requires the computation of an angular integral of the gravitational-wave energy flux (see, for example, Eq. (1) of Ref. [12]). Various approximations and models for this integral have appeared in the literature. Earlier works [13,14] have used a post-Newtonian quadrupolar approximation to compute displacement memory effects for BBH

*tislam@umassd.edu

inspirals. Subsequent studies [15–17] extended the memory calculation based on quadrupole modes to the full inspiral-merger-ringdown signal.

For purely numerical computations of the gravitational wave strain, Refs. [18,19] used detector-adapted coordinates and an approximate Isaacson stress-energy tensor to simplify angular integrals. The resulting kludge model [18,19] is very simple and applicable to higher harmonic modes, but due to these approximations it is mainly used to study memory phenomenology [20]. For example, this approach has been used to compute the memory effects for zoom-whirl extreme mass ratio inspirals (EMRI) orbits around fast spinning Kerr black holes [19]. Recently Talbot *et al.* [12] performed a direct computation of the memory up to $\ell = 4$ using full inspiral-merger-ringdown waveforms from numerical relativity simulations including many subdominant modes. This direct computation takes into account coupling between modes in the energy flux expression, and it is expected to be the most accurate because it introduces the fewest approximations. We note that NR techniques have largely been unable to extract memory modes [21], although recent advances [22] have made this possible by using the SpECTRE code's [23] Cauchy-characteristic extraction module [24].

Detectability of memory effects in current and future generation GW detectors has attracted significant interest [18,20,21,25–30]. In particular, Ref. [18] reports that third generation detectors will be able to detect memory effects from optimally oriented GW150914-like [31] events. Ref. [27] has considered detecting memory effects without being able to detect the "parent" oscillatory waveform while Ref. [26] looks for the evidence of memory in a population of GW150914-like BBH events. Recently Ref. [29] takes a different approach and attempts to infer a total memory observable from GW events. With current generation detectors, Ref. [28] finds that ∼2000 GW events need to be combined in order to recover strong evidence for memory effects in a binary population while Ref. [20] estimates that it would take ∼5 years of data for the memory modes to reach an SNR threshold of 3 in current detectors. Consistent with these expectations, no evidence of memory has been found in the population of the 50 GW BBH merger events reported in the first and second LIGO/Virgo gravitational-wave transient catalogs [32].

Previous studies have mostly focused on BBH systems that are representative of the events found in the first and second observing runs [1]. Similar to the first detection, GW150914, these are comparable mass, moderately (or non) spinning systems in quasicircular orbit. Here we consider heavy intermediate mass ratio inspirals (IMRIs) with the possibility of high spin and eccentricity. These binaries consist of an intermediate mass black hole (IMBH) with mass $\sim 10^2$–$10^4 M_\odot$ [33–35] paired with a first-generation black hole produced by stellar collapse of mass $\sim 4 - 40 M_\odot$. The resulting binaries will have a mass ratio in the range $q := m_1/m_2 = 2 - 10^4 : 1$ where m_1 (m_2) is the mass of the more (less) massive black hole. Evidence for IMBHs was previously known through indirect electromagnetic observations [35] and the low-end of this mass range has recently been confirmed by GW190521 [36]. The GW190521 remnant black hole has an estimated mass and dimensionless spin of $142^{+28}_{-16} M_\odot$ and $0.72^{+0.09}_{-0.12}$, respectively.

When formed through hierarchical mergers [37,38], for example when a GW190521-like remnant captures a stellar mass black hole, IMRI systems typically have a large total mass, large spin on the primary, and possibly residual eccentricity; features that potentially raise the prospect for memory detection especially when subdominant modes are included into the analysis [12,39]. On the other hand, a competing effect is that higher-mass-ratio sources emit weaker signals. A key goal of this paper is to explore the dependence of the memory's SNR as the total mass, spin, mass ratio, and eccentricity parameters are varied for different IMRI configurations similar to what might be expected if a GW190521-like remnant captured a stellar-mass BH. IMRIs are likely to exist in dense globular clusters and galactic nuclei [40,41] and are one of the prime sources for future-generation detectors [42,43]. In particular, IMRIs with total mass $< 2000 M_\odot$ may be detected by current-generation detectors [44] with higher mass binaries detectable by future space-based missions such as LISA [45] and beyond [46,47].

The rest of the paper is organized as follows. In Sec. II, we provide an overview of the models used to compute the memory effects. Section III describes our method for computing IMRI waveforms. In Sec. IV, we assess potential sources of systematic error in our memory computation. We then present results for the memory signal and its dependence on spin, eccentricity, and mass ratio (Sec. V) as well as the signal-to-noise ratio across different detectors. Finally, we discuss the implication of our results and caveats in Sec. VI.

II. NONLINEAR GRAVITATIONAL WAVE MEMORY MODELS

We model both the displacement and spin memory components. While displacement memory contributes predominantly to the $h^{\rm mem}_{20}$ and $h^{\rm mem}_{40}$ spherical harmonics modes (and therefore to plus polarization of the memory waveform), spin memory contributions show up in the $h^{\rm mem}_{30}$ mode (and therefore in the cross polarization) [25]. Below we describe the computation of both memory effects from a given oscillatory gravitational waveform.

A. Computing displacement memory

The nonlinear displacement memory sourced by gravitational waves can be computed using the expression [13,17,48]

$$h^{\mathrm{TT,dis}}_{jk}(T_r, r, \Omega) = \frac{4}{r}\int_{-\infty}^{T_r} dt \int_{S^2} d\Omega' \frac{dE}{dtd\Omega'}\left[\frac{n'_j n'_k}{1 - n'_l n^l}\right]^{TT}, \tag{1}$$

where r is the distance between the source and the observer, T_r is the retarded time, $\Omega = (\iota, \phi)$ are the angles (ι is the inclination angle between the angular momentum vector of the binary and the line of sight of the observer, ϕ is the reference phase at coalescence), and $n(\Omega)$ is the unit vector pointing from the source to the observer located at Ω. Here, Ω' coordinates describe the sphere over which the integral is taken and $n'(\Omega')$ is the associated unit vector.

The gravitational wave energy flux, $\frac{dE}{dtd\Omega}$, can be written in terms of the time-derivatives of the GW strain,

$$\frac{dE}{dtd\Omega} = \frac{r^2}{16\pi}\sum_{\ell',\ell'',m',m''} \langle \dot{h}_{\ell' m'} \dot{h}^*_{\ell'' m''}\rangle {}^{(-2)}Y_{\ell' m'} {}^{(-2)}Y^*_{\ell'' m''}, \tag{2}$$

expanded in spin-weighted spherical harmonics ${}^{(-2)}Y_{\ell m}$, where $\langle . \rangle$ denotes an average over a few waveform cycles[1] and $h^*_{\ell m}$ indicates the complex conjugate of $h_{\ell m}$. The memory expression in Eq. (1) is then projected onto the two orthogonal polarizations of the GWs by contracting with the complex polarization tensors e^{ij}_+, $e^{ij}_\times$:

$$h^{\mathrm{dis}} = h^{\mathrm{dis}}_+ - i h^{\mathrm{dis}}_\times = h^{\mathrm{TT,dis}}_{jk}(e^{jk}_+ - i e^{jk}_\times). \tag{3}$$

It is then convenient to expand the displacement memory

$$h^{\mathrm{dis}} = \sum_{\ell,m} h^{\mathrm{dis}}_{\ell m} {}^{(-2)}Y_{\ell m}, \tag{4}$$

in terms of spin-weighted spherical harmonics. Below we summarize three approximate methods used in the literature to compute Eq. (4).

1. Quadrupole approximation

This model uses the dominant (oscillatory) quadrupole mode h_{22} to compute the displacement memory contributions [17],

$$h^{(\mathrm{dis})}_{+22}(t) = \frac{1}{192\pi r}\Phi_1(\iota)\int_{-\infty}^{t} dt' |\dot{h}_{22}(t')|^2, \tag{5}$$

where $\Phi_1(\iota) \coloneqq \sin^2\iota(17 + \cos^2\iota)$, an overdot denotes differentiation with respect to t', and $|\cdot|$ denotes the complex modulus. For displacement memory sourced by the oscillatory (2,2) mode, $h^{(\mathrm{dis})}_{\times 22} = 0$. The quadrupole model has often been used to study the phenomenology of displacement memory [15,18,19].

2. Minimal waveform model

The minimal waveform model (*mwm*) [15] employs an analytical expression combining a PN approximation for the inspiral and a superposition of quasinormal modes during the merger and ringdown to compute the displacement memory both in time and frequency domain. The model has been calibrated to an effective-one-body (EOB) model to fit the nonlinear displacement memory in the comparable mass ratio regime. It is known that the *mwm* model over estimates the memory contribution [12,15,20]. Nonetheless, for the sake of completeness, in Sec. IV B we include this model in our comparison study.

3. Higher multipole model

The *higher multipole model*, derived by Talbot *et al.* [12], evaluates the expression in Eq. (4) by numerically integrating Eq. (1). The model uses both the quadrupole mode as well as available higher order modes up to $\ell = 4$ and accounts for the coupling between modes in the energy flux expression. The PYTHON package GWMemory [50] used to carry out the computation is publicly available.[2] Unless otherwise mentioned, we use this higher multiple model from GWMemory for calculating displacement memory. In Appendix A we compare GWMemory to two additional higher multipole memory models, finding that all three perform similarly.

B. Computing spin memory

Following [25], the spin memory

$$h^{(\mathrm{spin})}_{\times 22}(t) = \frac{3}{64\pi r}\Phi_2(\iota)\mathcal{I}(U^*_{22}\dot{U}_{22}). \tag{6}$$

is computed directly from the oscillatory (2,2) mode of the GW signal. Here, $\Phi_2(\iota) \coloneqq \sin^2\iota\cos\iota$, $\mathcal{I}$ denotes the imaginary part, and U_{22} is given by:

$$U_{22}(t) = \frac{1}{\sqrt{2}}[h_{22} + h^*_{2,-2}]. \tag{7}$$

III. IMRI WAVEFORM MODEL

Modeling the late inspiral and merger regimes from IMRI systems is challenging. One reason is that these systems are essentially inaccessible to exploration by numerical relativity codes due to the small length scale

[1] In practice, such waveform averaging has not been done in any of the models considered in this paper as the memory is known to be relatively insensitive to this procedure [49].

[2] The specific version of the code we use has a commit hash of 2a4b8084144b13a3f542b1e132d9bc629d4ec9c1. In particular, pull requests 7 and 19 correct various data files used in the memory computation. The paper's first version on the arXiv used a version of the code before pull request 7.

introduced by the lighter black hole. This is because the inspiral timescales linearly with q and finer grid resolution is required to resolve a smaller secondary. For these reasons the majority of NR simulations have had $q \leq 15$ [51,52] with a small handful of short-duration simulations performed at higher mass ratios [53]. As modern gravitational-waveform modeling efforts require NR data for calibration, a lack of NR data in this regime has prevented the construction of extensive and accurate models. One potential path forward was recently developed and applied to nonspinning, quasicircular BBH systems [54]. We now summarize our simple application of this technique to spinning and eccentric IMRI systems.

We generate our gravitational waveforms using black hole perturbation theory (BHPT). In this approach, the smaller black hole with a mass m_2 is modeled as a point particle, with no internal structure, moving in the spacetime of the heavier Kerr black hole with mass m_1 and spin angular momentum per unit mass a. The inspiralling trajectory of the particle is computed using standard energy and angular momentum balance equations [55–58]. To compute flux radiated to future null infinity and through the event horizon for the quasicircular inspirals we use the GREMLIN code [59–61] from the Black Hole Perturbation Toolkit [62]. For eccentric orbits we use Schwarzschild flux data which is available at Ref. [62], and we arrange the inspirals such that they fully circularize before the onset of the plunge. The inspiral trajectory is then extended to include the plunging trajectory [63–66]. With the complete trajectory in hand, the gravitational radiation is computed by numerically solving the time-domain Teukolsky equation in compactified hyperboloidal coordinates [67–70]. The resulting waveforms include the inspiral, merger, and ringdown of the binary. For an executive summary of the methods, see Sec. III of Ref. [19].

Waveforms computed as sketched above are suitable models for extreme mass-ratio inspirals where $q \gg 1$. Over the past decade, however, there has been mounting evidence that domain of validity of BHPT can be extended to include moderate mass-ratio binaries [71–74]. Recently it was shown waveforms from nonspinning, quasicircular binaries generated via BHPT can be made to agree remarkably well with NR waveforms with $q \sim 3$—15 via a simple change of the system's mass scale [54]. In order to model IMRIs we follow Ref. [54] and rescale the BHPT waveforms such that

$$h^{\ell m}(t; q, e_{\rm ref}, \chi) = \alpha h^{\ell m}_{\rm BHPT}(t\alpha; q, e_{\rm ref}, \chi), \tag{8}$$

where $h^{\ell m}_{\rm BHPT}$ are the spin-weight -2 spherical harmonic modes of the waveform computed from the Teukolsky solver. Here, $\chi = a/m_1$ is the dimensionless spin parameter of the heavier black hole, and $e_{\rm ref}$ is the eccentricity described in Sec. V D. We use $(\ell, m) = (2,2), (2,1), (3,3), (3,2), (3,1), (4,2), (4,3)$ modes in our computation. Negative m modes are computed using orbital plane symmetry, $h^{\ell,-m} = (-1)^l (h^{\ell m})^*$. The contribution of omitted higher order modes are negligible and these modes are often dominated by numerical error, and so we exclude them in this analysis.

The rescaling coefficient

$$\alpha(\nu) = 1 - 1.352854\nu - 1.2230006\nu^2 + 8.601968\nu^3 - 46.74562\nu^4, \tag{9}$$

used in Eq. (8) was obtained by fitting the (2,2)-mode BHPT waveforms against the (2,2)-mode NR data with nonspinning, quasicircular binaries from mass ratio $q = 3$ to $q = 10$, where $\nu = q/(1+q)^2$ is the symmetric mass ratio of the binary. The rescaled waveform was also shown to agree with a $q = 15$, nonspinning NR waveform not used in the fit with a mismatch value of 0.01 [54]. As the mass-ratio increases, the scaling factor α approaches unity thereby recovering the fiducial BHPT waveforms. The calibrated-BHPT waveform approach provides a method for computing IMRI waveforms in a regime currently inaccessible to NR simulations.

Thus far the α rescaling has only been determined for nonspinning, quasicircular binaries. Nonetheless we will use it to rescale the low eccentricity and spinning BHPT waveform data we use in this work. While we do not expect high-accuracy waveforms to be produced by this simple method, for our purpose it will be sufficient for surveying gravitational-wave memory from IMRIs as we demonstrate in Sec. IV.

IV. ROBUSTNESS STUDY

In this section we explore the robustness of our model for memory from IMRIs. In doing so, and for later sections, it will be useful to define the signal to noise ratio (SNR), ρ, via

$$\rho^2 = 4 \int_{f_{\rm min}}^{f_{\rm max}} \frac{|\tilde{h}(f)|^2}{S_n(f)} df, \tag{10}$$

where $S_n(f)$ is the one-sided noise power-spectral density of the detector, $\tilde{h}(f)$ is the Fourier transform of the detector response given by

$$h(t) = F_+ h_+ + F_\times h_\times, \tag{11}$$

and where F_+ and $F_\times$ are the antenna response functions of the detector. Our SNR computations will always use a single-detector configuration. The minimum and maximum frequencies, $f_{\rm min}$ and $f_{\rm max}$, in the limits of Eq. (10) are chosen to reflect the sensitivity bandwidth of the detector. For the detector configurations considered in this paper, we integrate over the frequencies 20 Hz to 1 kHz (for aLIGO and KAGRA [75]; 20 Hz is the default value used by LIGO

and Virgo during the two most recent observing runs [2,76]), 5 Hz to 1 kHz (for Einstein Telescope [77,78]), and 10 Hz to 1 kHz [for Cosmic Explorer [79–81]]. The lower frequency cutoff for ET and CE are subject to engineering uncertainties, although target design sensitivity values are consistent with ours. In future studies, it would be interesting to explore the impact of achievable sensitivity in the lower frequency band on the memory's SNR. Before transforming the time domain waveform to the frequency domain, we taper the time domain oscillatory waveform using a Planck window [82] while no tapering is used for the memory signal.[3]

A. Effect of truncating the weak field inspiral

Memory effects accumulate over the entire evolution of the binary and formally the lower limit of integration in Eq. (1) is negative infinity. However, we start the integration at the start of the waveform $t = -10,000M$, where $t = 0$ denotes the time at peak waveform amplitude and $M = m_1 + m_2$ is the total mass of the binary. We set the memory signal to zero at the start time. To obtain a physical strain, the dimensionless waveform is then appropriately scaled using total mass and distance. Unless otherwise specified, this prescription is applied throughout the paper.

In principle, one can use a PN correction to set a nonzero value for $h^{\rm dis}$ at $t = -10,000M$. We investigate whether such corrections are important to understand the detectability of memory signals. We generate displacement memory waveforms using the *mwm* model for a binary with $q = 10$, $M = 100M_\odot$, $D = 250$ Mpc and $\iota = \pi/4$. Throughout this paper, we use detector frame masses. In one case, we set the initial value of $h^{\rm dis}_{22}(t)$ to zero. In the other case, we allow the *mwm* waveforms to retain their nonzero values informed by PN terms. The waveforms yield an angle averaged SNR of 0.91 and 1.1 respectively in advanced LIGO detector indicating marginal differences in SNR. We therefore do not use any PN correction in our memory model.

B. Comparison between different displacement memory approximations

As a first look at our memory calculation, in Fig. 1 we plot the displacement memory computed using the three models described in Sec. II. For a fair comparison, we set $h^{\rm dis}_{22}(t)$ to be zero at the start of the waveform as described in Sec. IV A. We find that the time evolution of the memory waveforms are similar for all the models. However, memory computed from the quadrupolar mode generated through point-particle black hole perturbation theory exhibits slightly smaller values compared the higher multipole model. The *mwm* model, on the other hand, overestimates the memory effects. This is not unexpected as the *mwm* model is calibrated for binaries with equal masses and/or small spins. Similar results were found in, e.g., Ref. [20]—see their Fig. 1.

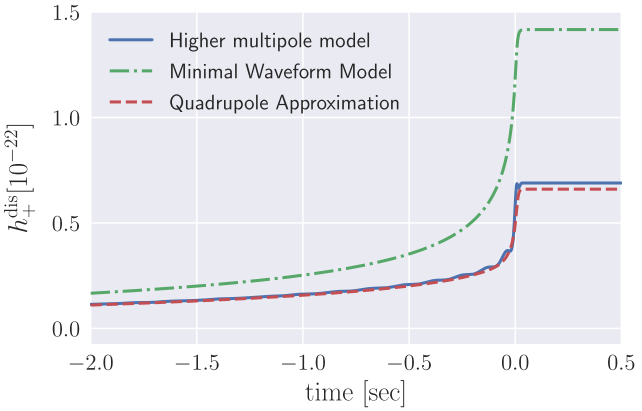

FIG. 1. Displacement memory $h^{\rm dis}(t)$ for a nonspinning BBH with total mass $M = 200M_\odot$, mass ratio $q = 10$, a luminosity distance $D = 250$ Mpc, and at an inclination $\iota = \pi/4$ computed using the three models described in Sec. II A. Unless otherwise specified, we use detector-frame masses throughout this paper. As has been previously noted [20], the *mwm* (dash-dot green line) overestimates the displacement memory effect. The memory signal computed from the dominant (2,2) mode (dashed red line) slightly underestimates the effect as compared to a computation using all available modes (solid blue line). The results of our paper use the higher multipole model [12,50] as it is expected to be the most accurate.

C. Comparison between displacement memory effects computed using ppBHPT and NR waveforms in the comparable mass ratio regime

As a second check on our memory calculation, we compute the memory modes for different binaries in the small mass ratio regime ($1 \le q \le 10$) while fixing $M = 200M_\odot$, $\chi = 0.0$, $e_{\rm ref} = 0.0$ and $D = 250$ Mpc. We perform this analysis with two different waveform families: a hybridized EOB-NR based aligned-spin surrogate model `NRHybSur3dq8` [87] and `EMRISur1dq1e4` [54], a surrogate version of the ppBHPT waveforms calibrated to NR.

Figure 2 shows the dominant (2,0) memory mode along with two important subdominant modes. For `NRHybSur3dq8`, we compute the memory modes for $1 \le q \le 9$ and, for `EMRISur1dq1e4`, we show the results for

[3]We note that the SNR can vary significantly depending on the choice of tapering strategy and/or data analysis strategy, detector, and source parameters; for example, see Fig. 1 of Ref. [83] or Appendix A of Ref. [84]. In general, SNR calculations using Eq. (10) that omit tapering will overestimate the SNR due to spurious high-frequency features. This unphysical behavior can be understood by noting that (i) the displacement memory's periodic extension (as assumed by the Fourier transform) leads to a discontinuity of size $h^{\rm dis}(t_{\rm end})$, and (ii) the Fourier transform of a step function is proportional to $1/f$. Alternatively, one can use entirely different data analysis strategies that are designed to handle signals that do not go to zero [85,86].

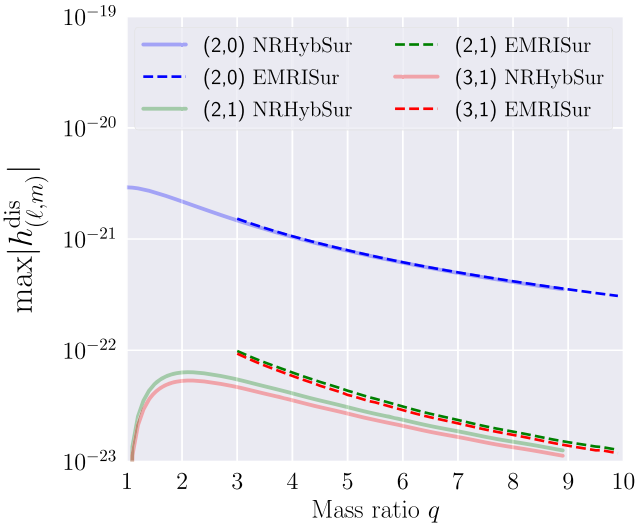

FIG. 2. Maximum amplitude of three different memory modes as a function of mass ratio. We compute the displacement memory using two different waveform models: EOB-NR hybridized aligned spin surrogate waveform `NRHybSur3dq8` (*solid lines; labeled as* `NRHybSur`) and an α-calibrated ppBHPT waveform from the surrogate model `EMRISur1dq1e4` (*dashed lines; labeled as* `EMRISur`). We observe a reasonable match between the memory effects computed with these two different models (details in text; Sec. IV C).

$q \geq 3$ to reflect their respective domains of validity. The figure shows visual consistency in the computation of (2,0) memory mode, but noticeable discrepancies for these subdominant modes. Differences in the higher order memory modes arise as the higher order oscillatory modes in the α-calibrated ppBHPT waveforms are not individually tuned to NR. Similarly, small (but noticeable) differences in the (2,0) mode are due to mode coupling between the subdominant oscillatory modes that arise in the evaluation of Eq. (2); Sec. IV D considers a memory computation using only the quadrupole oscillatory mode where we no longer find any discrepancies.

The small differences shown in Fig. 2 are not a concern for our SNR computations as the (2,0) memory mode is expected to be dominant over other higher order memory modes (see Figs. 9 and 10). We also observe that the differences in the higher order modes decrease as mass ratio increases as the ppBHPT framework is expected to perform better in the high mass ratio regime that we are interested in. Interestingly, we observe that the higher order memory modes have a maxima around $q \sim 2$. This is consistent with the findings of Talbot *et al.* [12] who observe a growth in the maximum of the (2,1) and (3,1) memory modes as q increases from 1 to 2 (cf. Fig. 3 of Ref. [12]). While we have not explored the origin of this behavior, we note that for nonspinning BBH systems in quasicircular orbit, the odd-m oscillatory modes' amplitude are zero at $q = 1$, turn on quickly as q becomes nonunity, and then transition to $\propto 1/q$ behavior as q becomes large.

Further calibration of the higher order radiative modes in the `EMRISur1dq1e4` model [88] will improve the agreement between the two models for the higher order memory modes. The comparison in this section for $q \leq 10$ shows a good agreement for the dominant (2,0) memory mode and reasonable qualitative agreement for the subdominant memory modes. As both models are calibrated to NR simulations for $q \leq 10$, we next consider mass ratios $q \geq 10$.

D. Comparison between displacement memory effects computed using α-calibrated ppBHPT and EOB waveforms in intermediate mass ratio regime

As discussed in Sec. III there are essentially no NR simulations of IMRIs. In lieu of direct comparison to NR, to explore the robustness of our memory calculation for IMRIs we now compute displacement memory for mass ratios $3 \leq q \leq 100$ using the α-calibrated ppBHPT waveforms and an aligned-spin EOB model `SEOBNRv4HM` [89]. By construction both models give the correct result in the geodesic, $q \to \infty$, limit, both include some information from linear-in-the-mass-ratio BHPT, and both are calibrated against NR simulations for $q \leq 10$. Neither model

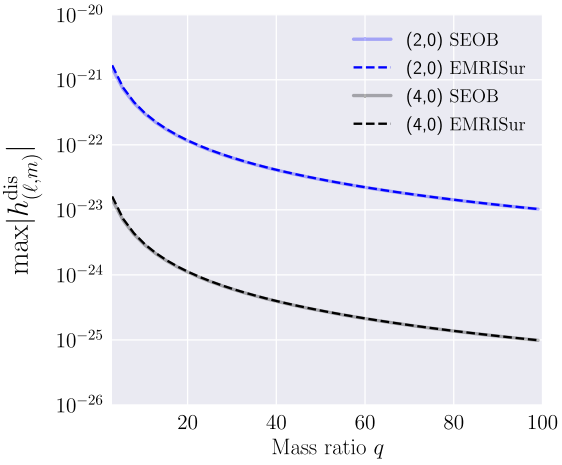

FIG. 3. Maximum amplitude of two different memory modes as a function of mass ratio. We compute the displacement memory using two different waveform models: an aligned-spin EOB model `SEOBNRv4HM` (*solid lines; labeled as* `SEOB`) and a ppBHPT-based surrogate waveform `EMRISur1dq1e4` (*dashed lines; labeled as* `EMRISur`). We fix $M = 200M_\odot$, $\chi = 0.0$, $e_{\rm ref} = 0.0$ and $D = 250$ Mpc. We find the relative difference for the maximum displacement memory computed using these two models is always less than 1% for both the (2,0) and (4,0) memory modes. The observed agreement between these two different models in both small and intermediate mass ratio regime gives us confidence that the memory effects computed for IMRIs using either `EMRISur1dq1e4`, `SEOBNRv4HM`, or α-calibrated `ppBHPT` waveforms accurately capture the true displacement memory in this regime.

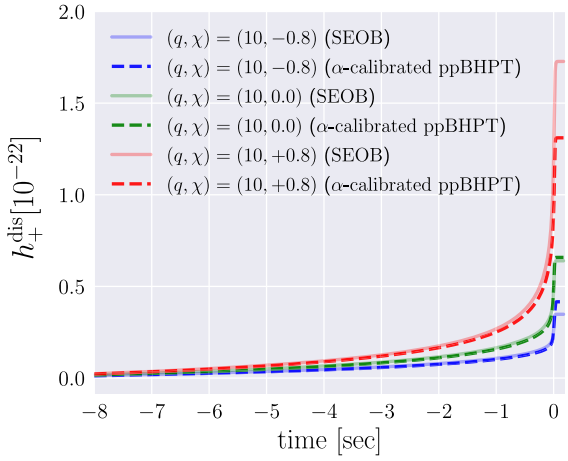

FIG. 4. Displacement memory for three different spin configurations $\chi = \{-0.8, 0.0, +0.8\}$ with mass ratio $q = 100$, $M = 200M_\odot$, $\chi = 0.0$, $e_{\rm ref} = 0.0$ and $D = 250$ Mpc. We compute the displacement memory using two different waveform models: an aligned-spin EOB model `SEOBNRv4HM` (*solid lines; labeled as* `SEOB`) and a α-calibrated ppBHPT waveforms (*dashed lines; labeled as* `α-calibrated ppBHPT`). For $\chi = +0.8$, final displacement memory value between SEOB and `α-calibrated ppBHPT`) are a bit different. Otherwise, relative differences between the displacement memory profiles from these two models are always less than 8%. The observed agreement between the memory effects computed with these two different models gives us confidence that the memory effects computed for IMRIs using `SEOBNRv4HM` or the α-calibrated `ppBHPT` waveforms accurately capture the true displacement memory in this regime.

is calibrated in the IMRI regime but we find the two models provide similar memory computations from binaries with mass ratios $q \leq 100$. To demonstrate this we use the dominant quadrupolar mode to calculate the memory effects. In Fig. 3, we show the maximum amplitude of the displacement memory as a function of mass ratio q where we fix $M = 200M_\odot$, $\chi = 0.0$, $e_{\rm ref} = 0.0$, and $D = 250$ Mpc. Up to $q = 100$ we find the relative difference for the maximum displacement memory computed using the two models is always less than 3% for the dominant (2,0) memory mode.

We now consider the consistency between the two models when the larger black hole is spinning. In this portion of the parameter space the SEOBNRv4HM model has been calibrated using spinning NR simulations. On the other hand the α-calibrated ppBHPT model computes the GWs from an inspiral into a Kerr black hole in the extreme mass ratio limit and then rescales to the waveform for IMRIs using the parameter α which is fitted to NR data for *nonspinning* binaries. Nonetheless we find that the memory computed for spinning binaries using the α-calibrated ppBHPT and SEOBNRv4HM models continue to agree well for spinning binaries. In Fig. 4 we show the total displacement memory computed using the two models for three different spin configurations $\chi = \{-0.8, 0.0, +0.8\}$ for mass ratio $q = 10$. All other parameters have remained the same as those reported in the previous paragraph.

The observed agreement between these two models gives us confidence in the memory effects computed from both in the IMRI regime. It is worth noting that while we find that the memory computed using the α-calibrated ppBHPT and SEOBNRv4HM models agree across a wide range of mass ratios, this does not imply the oscillatory waveforms themselves will necessarily agree. This can be seen directly from Eq. (2), which is less sensitive to small dephasing than the overlap integral commonly used to compare waveform models.

E. Comparison between spin memory effects computed using different waveform models

As a final sanity check, we compute the spin memory for a binary with mass ratio $q = 10$, $M = 200M_\odot$, $e_{\rm ref} = 0.0$, and $D = 250$ Mpc. We restrict ourselves to a nonspinning system so that we can generate a high-accuracy `NRHybSur3dq8` waveform, which can be extrapolated to $q = 10$ with higher accuracy provided $\chi = 0$. In Fig. 5, we show the spin memory effect computed using `SEOBNRv2`, `NRHybSur3dq8`, and the α-calibrated ppBHPT waveform based surrogate model `EMRISur1dq1e4`. Maximum relative differences between the spin memory computed using `EMRISur1dq1e4` and `NRHybSur3dq8` (or `SEOBNRv2`) is always ≤15%.

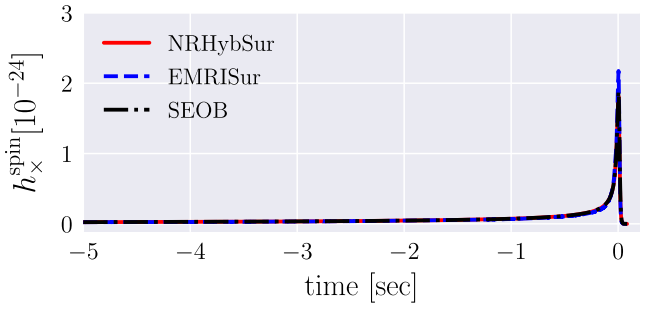

FIG. 5. Spin memory computed for a nonspinning binary with mass ratio $q = 10$ using three different waveform models: an aligned-spin EOB model `SEOBNRv4HM` (dashed dotted lines; labeled as `SEOB`), an EOB-NR hybridized aligned spin surrogate waveform `NRHybSur3dq8` (solid lines; labeled as `NRHybSur`), and a α-calibrated ppBHPT waveform from the surrogate model `EMRISur1dq1e4` (dashed lines; labeled as `EMRISur`). We fix $M = 200M_\odot$, $e_{\rm ref} = 0.0$ and $D = 250$ Mpc. Relative differences between the spin memory computed using these models are always less than 15%. The observed agreement between the spin memory effects computed with these three different models gives us confidence that the memory effects computed for IMRIs using either `NRHybSur3dq8`, `SEOBNRv4HM`, or the α-calibrated `ppBHPT` waveforms accurately capture the true spin memory in this regime.

V. PHENOMENOLOGY & DETECTABILITY

In this section, we explore the memory phenomenology and detectability as the mass ratio, spin, and eccentricity is varied. We report SNRs computed using the design sensitivity of detectors including advanced LIGO, Cosmic Explorer (CE), and Einstein Telescope (ET). Assuming Gaussian detector noise, an SNR of ≈ 5 is typically considered sufficient for detection. For multiple stacked detections some authors have considered a total memory SNR value as low as 3 to be sufficient for claiming hints of memory [18,20,26]. We note that untapered displacement memory waveforms are used in our study (cf. footnote 3).

For most of our SNR results, we fix the intrinsic BBH parameters and luminosity distance, D, and report the maximum and angle-averaged SNR values. To compute the angle-averaged SNR, we simulate a total of 1125 signal realizations where we sample right accession α and polarization ψ uniformly in $[0, 2\pi]$, declination δ and inclination ι uniformly in $\cos\delta$ and $\cos\iota$ from $[-1, 1]$. The maximum SNR is taken to be the largest value over the 1125 signal realizations. As the SNR is proportional to 1/D, our SNR results can easily be scaled to different luminosity distance values. Our default choice of $D = 250$ Mpc is motivated by the inferred distance for the event GW190814 [90], highest mass ratio event ($q \sim 10$) detected by LIGO/Virgo so far. As GW190814 is one of the closest BBH detections to date, our choice of $D = 250$ Mpc is represents a plausibly optimistic default value. While we will broadly consider IMRI systems, one particular focus is on memory from hierarchical mergers involving second- or third-generation black holes. These systems present, on average, both larger masses and larger spins [38]. Many of our experiments consider systems with $M = 200M_\odot$, $q = 10$, and large-spin systems, which is consistent with a GW190521-like remnant capturing a first-generation, stellar-mass black hole.

A. Structure of the memory signal

To understand the structure of memory waveforms, we pick a nonspinning GW signal with mass ratio $q = 10$, total mass $M = 200M_\odot$ and luminosity distance $D = 250$ Mpc. In Fig. 6, we plot both the displacement memory (middle panel) and spin memory (lower panel) contributions from the dominant $\ell = 2$, $m = 2$ mode. For comparison, we also show $\ell = 2$, $m = 2$ mode waveform (*upper panel*). We fix the inclination to be $\iota = \pi/4$ such that the memory effect fits in between the maximum and conservative cases (discussed more in Fig. 8). Displacement memory effects are found to be two orders of magnitude smaller than the oscillatory waveform, and the spin memory contributions are another $\sim$ two orders of magnitude smaller compared to its displacement memory counterpart. We note that the displacement memory

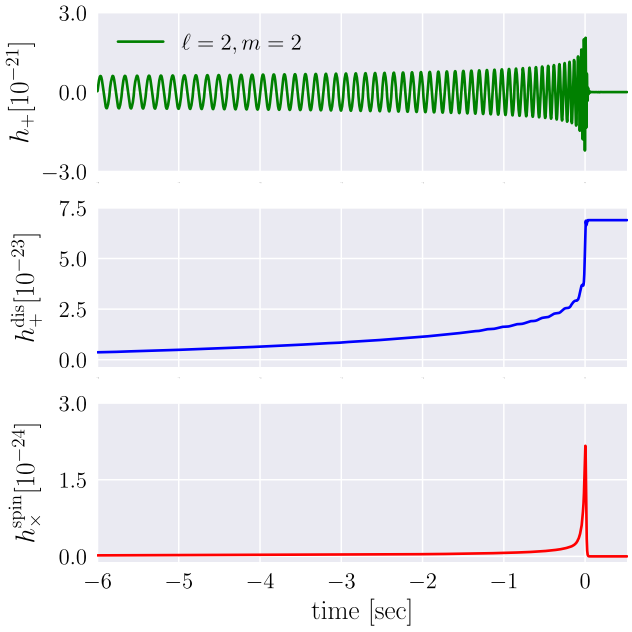

FIG. 6. Upper panel: plus polarization of the h_{22} spherical harmonic mode for a nonspinning BBH with total mass $M = 200M_\odot$, mass ratio $q = 10$ at a luminosity distance $D = 250$ Mpc and at an inclination $\iota = \pi/4$. Middle panel: gravitational waveforms associated with the nonlinear displacement memory contributions computed using all available modes using the higher multipole model. Lower panel: spin memory contributions computed from the dominant $\ell = 2$, $m = 2$ mode.

increases gradually during the inspiral and reaches a flat maximum following the merger. Spin memory, on the other hand, drops sharply after the merger.

In Table I we report the maximum and angle-averaged SNR for a BBH with $q = 10$, $M = 200M_\odot$ and $D = 250$ Mpc in four different detectors. We find that while displacement memory modes will have significant SNRs in future detectors and could possibly result in confident detection, spin memory modes would still have very low SNRs. These SNR values are consistent with earlier studies done in the context of comparable mass binaries [18,25,27].

To probe the effects of higher modes, in Fig. 7 we show the total memory computed using different mode content for a binary with $q = 10$ and $M = 200M_\odot$. To compute the displacement memory we use (i) only the dominant $(2, \pm 2)$ modes (solid red line), (ii) all modes with $\ell \leq 2$ (dashed green line), (iii) all modes with $\ell \leq 3$ (dash-dot blue line), (iv) and all modes in our α-calibrated ppBHPT waveforms (dashed black line). We notice that the memory contribution from the quadrupolar mode already accounts for most of the signal content. To quantify the importance of the higher modes in the memory computation we compute SNRs of displacement memory signals obtained using only the quadrupolar mode (Table I; in parenthesis). We find that SNRs increase by about $\sim$7% across detectors when higher order modes are included in memory computation.

TABLE I. Angle-averaged and maximum SNRs[a] of the displacement memory mode and spin memory mode in different detectors (aLIGO, KAGRA [75], ET and Cosmic Explorer (CE) [79]). For all detectors, we use their design sensitivity. The BBH source parameters are: $q = 10$, $M = 200M_\odot$, $D = 250$ Mpc. For a comparison we also show the SNRs (in parenthesis) for memory signals computed using only the dominant $l = 2, m = \pm 2$ mode. We note that SNRs for the displacement memory are likely overestimated due to the issue mentioned in footnote 3.

	Displacement Memory		Spin Memory	
	$\rho_{\rm avg}$	$\rho_{\rm max}$	$\rho_{\rm avg}$	$\rho_{\rm max}$
aLIGO	0.39 (0.38)	1.69 (1.63)	0.001	0.009
KAGRA	0.29 (0.28)	1.24 (1.19)	0.001	0.004
Virgo	0.316 (0.308)	1.367 (1.194)	0.001	0.005
ET	4.46 (4.30)	19.29 (18.42)	0.03	0.19
CE	14.91 (14.18)	64.85 (60.748)	0.12	0.81

[a]Symbols: $\rho_{\rm avg}$: average SNR; $\rho_{\rm max}$: maximum SNR.

We now probe the dependence of both the displacement and spin memory on the inclination angle ι. In Fig. 8, we plot the maximum of the displacement and spin memory computed using all available modes as a function of the ι. We fix $q = 10$, $M = 200M_\odot$, and $D = 250$ Mpc. We find that the maximum effects for the displacement memory is obtained for $\iota = \pi/2$ whereas spin memory modes are loudest for $\iota \sim \pi/4 - \pi/3$. This is due to the fact that for the displacement memory the (2,0) mode is dominant over other modes, and the angular dependency of a waveform consisting of the (2,0) mode only is proportional to $\sim \sin^2 \iota$ (as done in quadrupole approximation).

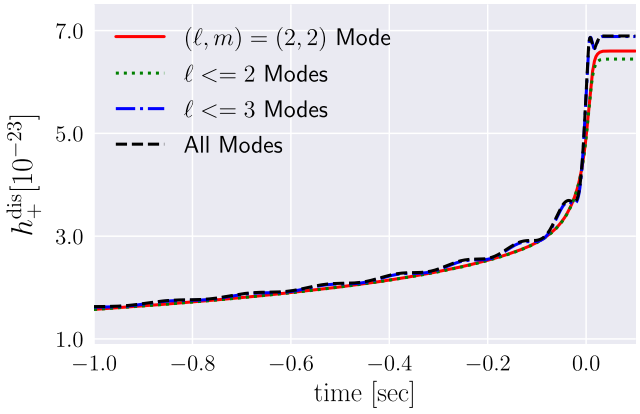

FIG. 7. Gravitational waveform associated with the nonlinear displacement memory contributions computed using different combinations of spherical harmonics modes. Our system is a nonspinning BBH with total mass $M = 200M_\odot$, mass ratio $q = 10$ at a luminosity distance $D = 250$ Mpc and at an inclination $\iota = \pi/4$. We zoom in the late inspiral, merger and ringdown part of the waveform.

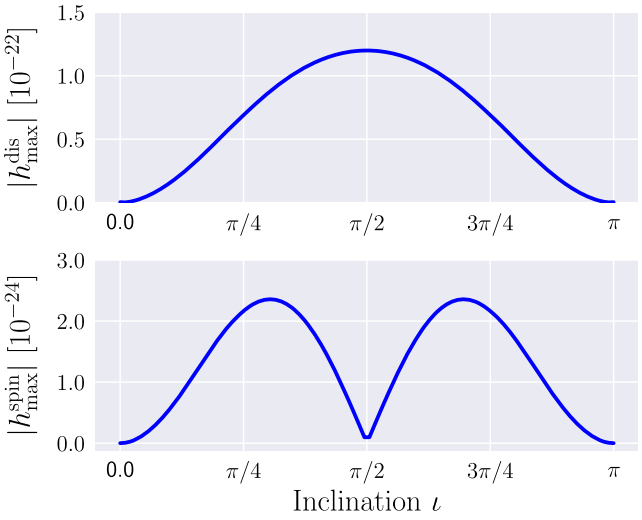

FIG. 8. Maximum of the total displacement memory and spin memory as a function of the inclination angle ι. Our system is a nonspinning BBH with total mass $M = 200M_\odot$, mass ratio $q = 10$ at a luminosity distance $D = 250$ Mpc.

B. Mode decomposition of the memory waveform

Following the prescription provided in Ref. [12], we decompose the memory waveform into spin-weighted harmonics modes to explore their dependence on spin and eccentricity (Fig. 10), and mass ratio (Fig. 9). In all cases, as is well known, we find that the (2,0) mode is dominant. Many of the subdominant modes [except the (2,1) and (3,1)] are negligible compared to the (2,0) mode and could safely be ignored for SNR computations, although we will continue to include them. We further find that (ℓ, m) and $(\ell, -m)$ memory modes have exactly same maximum amplitudes, as we would expect for systems that obey orbital-plane symmetry.

Figure 9 shows the mode decomposition of $q = 10$ binaries while varying spin and eccentricity configurations. By comparing the quasicircular (blue circle) and eccentric (red triangle) cases, we see that eccentricity brings almost no change in the maximum value of the memory modes. This has been observed for the dominant (2,0) memory mode in the context of comparable mass ratio binaries [39,49], and our result extends this finding in the intermediate mass ratio regime and for the subdominant memory modes. Spinning systems, however, have noticeably different mode content as compared to their nonspinning counterparts; Sec. V C considers the impact of spin on the memory's SNR.

Figure 10 shows the different memory modes for nonspinning, noneccentric binaries as the mass ratio is increased. The effect of mass ratio is clearly observed in

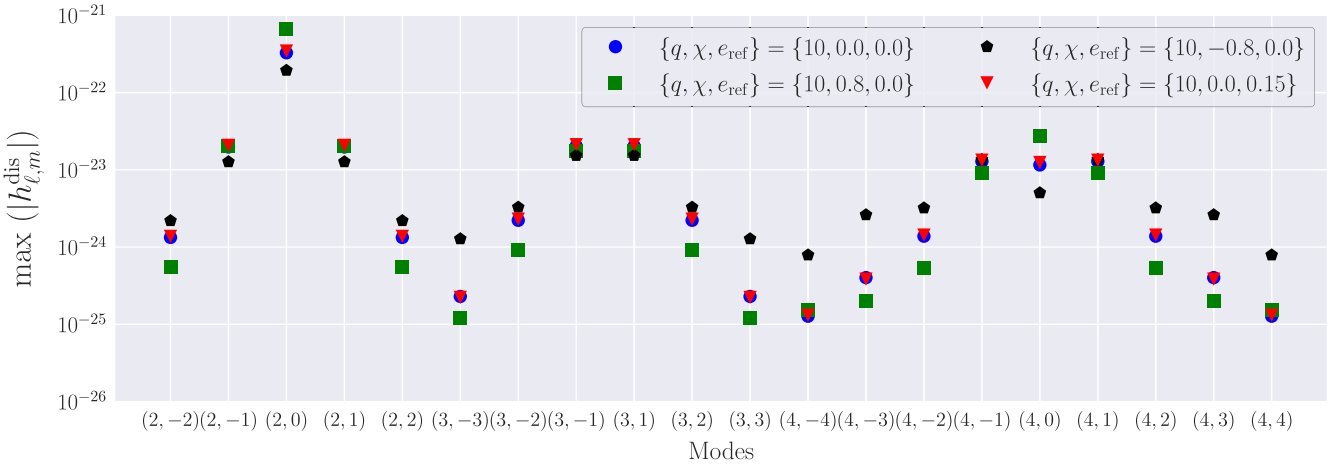

FIG. 9. The spherical harmonic decomposition of the displacement memory waveform for different spin and eccentric configurations. We fix mass ratio $q = 10$, $M = 200M_\odot$ and $D = 250$ Mpc. The absolute value of the late-time memory is shown as a function of the (ℓ, m) spherical harmonic decomposition of the memory. This figure extends Fig. 3 of Talbot *et al.* [12] in the high mass ratio regime—focusing on mass ratio $q = 10$ and for different configurations of spins and eccentricities. The (3,0) mode's amplitude is extremely small and omitted from this figure.

Fig. 10 where the maximum value in all of the memory modes decreases with mass ratio. Reference [12], however, observed an increased contribution to higher order modes from the $q \leq 2$ asymmetric mass binaries they considered, which is also apparent in Fig. 2.

C. Effect of spin

Next, we provide a systematic study of both displacement and spin memory's spin dependence. We compute the memory effects for a set of binaries with mass ratio $q = 10$ but for different values of the primary black-hole's dimensionless spin χ. We fix $q = 10$, $M = 200M_\odot$, $D = 250$ Mpc and $\iota = \pi/4$. In Fig. 11, we show the displacement and spin memory effects as a function of time for three different BBH with spins $\chi = [-0.8, 0.0, 0.8]$. We observe that the memory effect increases as the spin χ increases. This is due to the fact that prograde inspiral spends a longer in the strong field as the last stable orbit's radius shrinks. As a consequence, the SNR of emitted GWs is also expected to be larger than the corresponding nonspinning binary system. Our findings are consistent with results obtained in Ref. [19] that observes an increased memory amplitude for lager values for spins.

In Fig. 12, we report the maximum and angle-averaged SNR for the memory modes in a BBH with $q = 10$, $M = 200M_\odot$ and $D = 250$ Mpc. The maximum SNRs for the displacement memory in ET is sufficient for confident detection across the entire range of spins considered here. The angle-averaged SNR for the displacement memory is

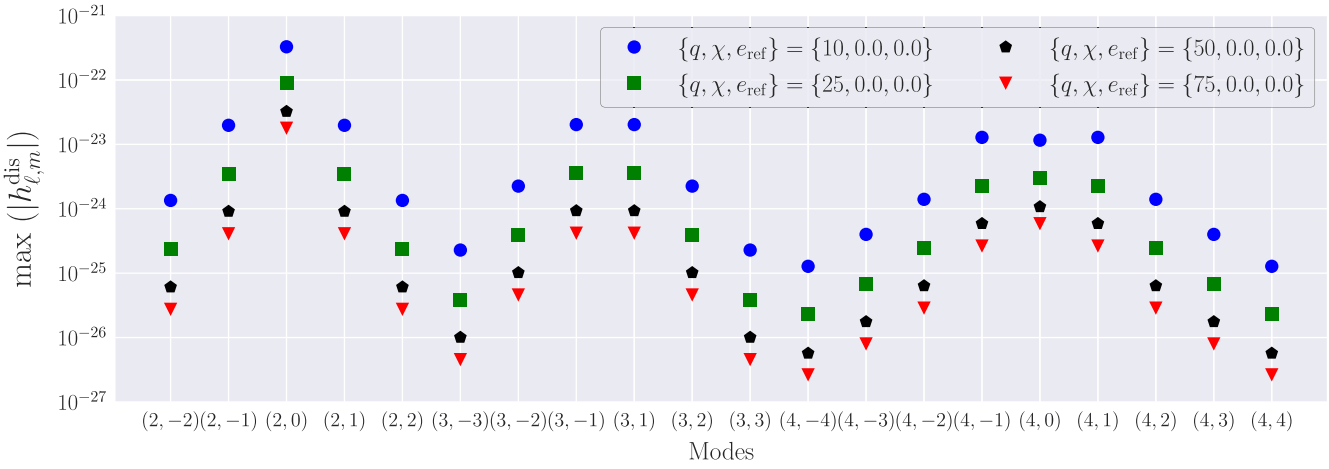

FIG. 10. The spherical harmonic decomposition of the displacement memory waveform for different mass ratios. We fix spin $\chi = 0.0$, $e_{\rm ref} = 0.0$, $M = 200M_\odot$ and $D = 250$ Mpc. The absolute value of the late-time memory is shown as a function of the (ℓ, m) spherical harmonic decomposition of the memory. This figure extends Fig. 3 of Talbot *et al.* [12] in the high mass ratio regime—covering mass ratios $10 \leq q \leq 75$. The (3,0) mode's amplitude is extremely small and omitted from this figure.

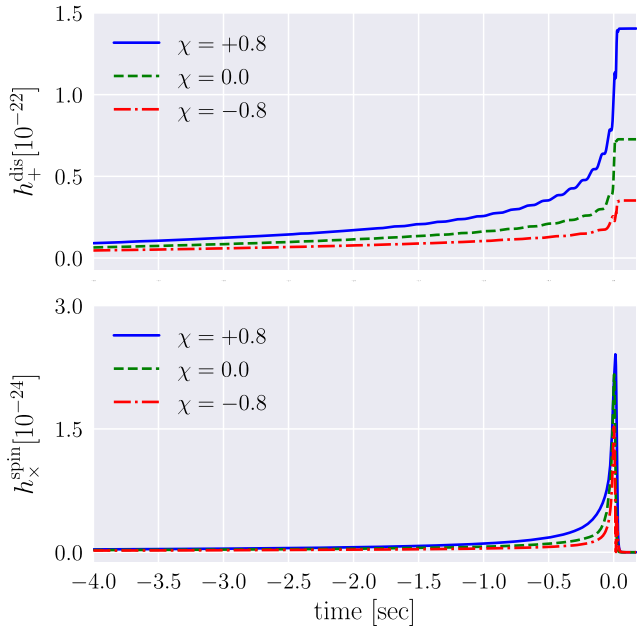

FIG. 11. Time evolution of the displacement memory $h^{\rm dis}(t)$ (upper panel) and spin memory $h^{\rm spin}(t)$ (lower panel) for three different spin values, χ, of the primary black hole. Our system is a BBH with total mass $M = 200M_\odot$, mass ratio $q = 10$ at a luminosity distance $D = 250$ Mpc and inclination $\iota = \pi/4$.

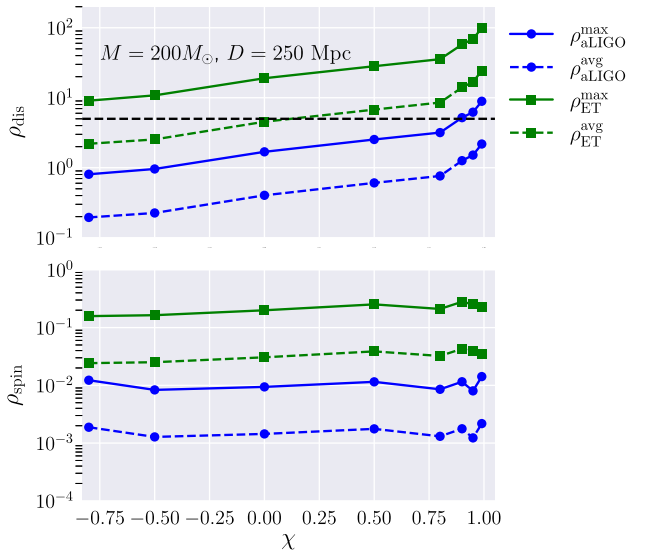

FIG. 12. Maximum SNR $\rho_{\rm max}$ (solid line) and angle-average SNR $\rho_{\rm avg}$ (dashed line) for the memory modes computed using the design sensitivity of the advanced LIGO (blue) and ET (green) as a function of the spin on the primary black-hole. We use $q = 10$, $M = 200M_\odot$ and $D = 250$ Mpc. Upper panel (lower panel) shows the SNR for the displacement memory (spin memory). Black dashed line denotes an SNR of 5, typical threshold for detection. We note that SNRs for the displacement memory are likely overestimated due to the issue mentioned in footnote 3.

between ∼1 (for $\chi = -0.8$) and ∼20 (for $\chi = 0.99$). For hierarchical mergers with second-generation (or higher) component black holes, spins of up to $\chi \approx 0.9$ are expected [37,38], suggesting that memory from some of these system may be directly observed with ET even in the typical case. Indeed, a handful of high-spin black holes have been identified [91,92] and may therefore be the most promising candidates for memory detections. For aLIGO, angle-averaged SNRs are always below the value 5 at our fiducial distance $D = 250$ Mpc, although optimally oriented binaries cross the detection threshold for $\chi >= 0.9$. Increased SNR at larger spin values would therefore favorably contribute to forecasts for memory detection. The spin memory, however, is unlikely to be detected in aLIGO or ET.

D. Effect of eccentricity

Depending on the formation channel, some IMRIs are expected to retain significant eccentricity even at the final stage of the inspiral [42,93,94]. Memory from eccentric systems has typically been studied using PN approximations [49,95] or using a kludge model [19]. In this paper we use the higher multipole model and focus on small to moderate eccentricities with $e \lesssim 0.2$. To estimate the eccentricity at a given time, we use [96]:

$$e(t) = \frac{\sqrt{\omega_p(t)} - \sqrt{\omega_a(t)}}{\sqrt{\omega_p(t)} + \sqrt{\omega_a(t)}}, \tag{12}$$

where ω_a and ω_p are the orbital frequencies at apocenter and pericenter, respectively. We let $e_{\rm ref}$ be the value of $e(t)$ measured three cycles before the merger. A detailed description of the method is given in Refs. [96,97].

We explore how the memory effect changes as the binary becomes increasingly more eccentric. To do this, we simulate gravitational waveforms for $q=10$, $M=200M_\odot$, $D = 250$ Mpc, and $\iota = \pi/4$ with different values of eccentricity. In Fig. 13, we show the memory contributions as a function of time for one particular value of eccentricity $e_{\rm ref} = 0.17$. Eccentricity introduces additional modulation in both displacement and spin memory components. Such modulations are small in the displacement memory but prominent for the spin memory. The modulations are strongly correlated to the modulations in the oscillatory gravitational waveform (upper panel; Fig. 13) and these features become more evident as the eccentricity increases (Fig. 14). For the displacement memory, these modulations roughly resembles the staircase structure found in the zoom-whirl orbits [19]. These modulations are consistent with results obtained in Refs. [39,49] for comparable mass ratio binaries.

Next, we compute the SNRs for memory signals from eccentric binaries. In Table II we report SNRs for the binary with highest eccentricity ($e_{\rm ref} = 0.17$) considered in our study. For comparison, we also show the SNR values computed for the noneccentric binary. The SNR values

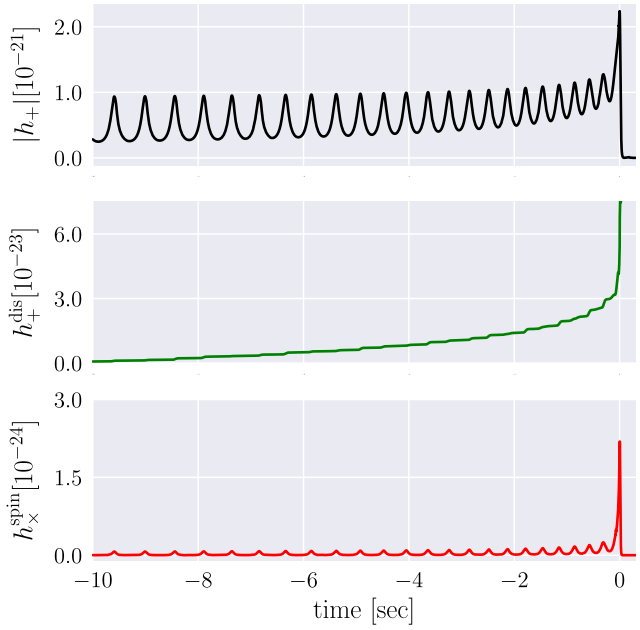

FIG. 13. Time evolution of the displacement memory $h^{\rm dis}(t)$ (middle panel) and spin memory $h^{\rm spin}(t)$ (lower panel) for the BBH with eccentricity $e_{\rm ref} = 0.17$ measured three cycles before the merger. All other details are same as in Fig. 6. For a comparison, we show the time evolution of the $\ell = 2$, $m = 2$ mode amplitude in the upper panel. Eccentricity introduces additional modulation in both the amplitude of $\ell = 2$, $m = 2$ oscillatory mode and both flavors of memory.

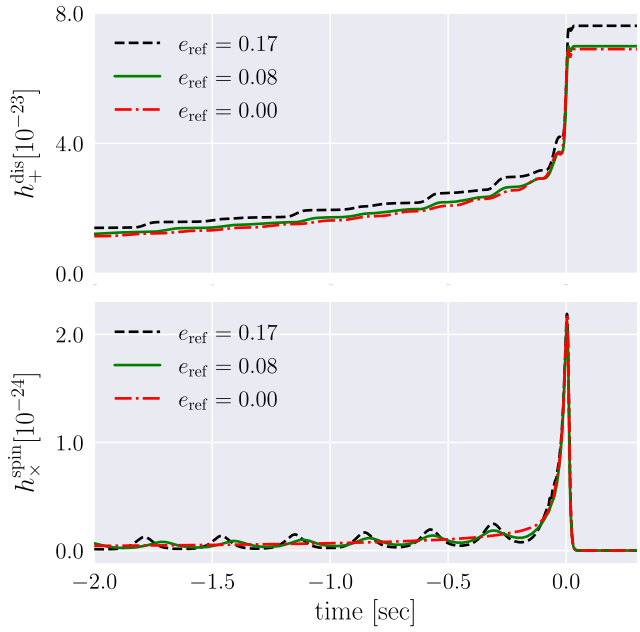

FIG. 14. Time evolution of the displacement memory $h^{\rm dis}(t)$ (upper panel) and spin memory $h^{\rm spin}(t)$ (lower panel) for three different eccentricity values $e_{\rm ref}$. Our system is a BBH with total mass $M = 200M_\odot$, mass ratio $q = 10$ at a luminosity distance $D = 250$ Mpc and inclination $\iota = \pi/4$.

TABLE II. Angle-averaged and maximum SNRs of the displacement memory mode and spin memory mode in different detectors for a $M = 200M_\odot$, $\chi = 0.0$, $D = 250$ Mpc binary with highest eccentricity ($e_{\rm ref} = 0.17$) considered in our study. For all detectors, we use their design sensitivity. For a comparison, we also show the SNRs of the corresponding noneccentric binary in parenthesis. We note that SNRs for the displacement memory are likely overestimated due to the issue mentioned in footnote 3.[a]

	Displacement Memory		Spin Memory	
	$\rho_{\rm avg}$	$\rho_{\rm max}$	$\rho_{\rm avg}$	$\rho_{\rm max}$
aLIGO	0.409 (0.39)	1.772 (1.69)	0.001 (0.001)	0.010 (0.009)
KAGRA	0.298 (0.29)	1.290 1.235	0.001 0.001	0.004 0.004
Virgo	0.330 (0.316)	1.427 (1.367)	0.001 (0.001)	0.005 (0.005)
ET	4.64 (4.46)	20.140 (19.295)	0.031 (0.031)	0.201 (0.199)
CE	15.516 (14.915)	67.632 (64.848)	0.125 (0.124)	0.817 (0.810)

[a]Symbols: $\rho_{\rm avg}$: average SNR; $\rho_{\rm max}$: maximum SNR.

change by at most 4 percent. We find that for a given mass ratio and detector sensitivity, the computed SNRs are roughly constant for $e_{\rm ref} \leq 0.17$ despite the rich phenomenology that larger eccentricity offers. This is perhaps not surprising in light of the fact that most of the SNR is accumulated around the merger, and maximum value for the memory signal changes modestly with eccentricity for the values of $e_{\rm ref}$ considered here. We further confirm that the differences in SNR computed using ppBHPT waveforms with and without α scaling [defined in Eq. (8)] are small, suggesting that the rescaling obtained from the noneccentric binaries can reasonably be used for eccentric binaries—at least for the purpose of this study.

E. Effect of mass ratio

We explore how the memory effect changes as the binary becomes increasingly asymmetric. To do this, we simulate gravitational waveforms with $M = 200M_\odot$, $\chi = 0.0$, $e_{\rm ref} = 0.0$, $D = 250$ Mpc and $\iota = \pi/4$ while varying the mass ratio. In Fig. 15, we plot both the displacement memory and spin memory for three different mass ratios $q = \{10, 15, 25\}$. The memory signals become weaker as the mass ratio increases, which follows from the fact that the oscillatory mode's amplitude decreases as $1/q$ in the large-mass-ratio limit. In Fig. 16, we show the maximum and angle-averaged SNR for memory signals with different mass ratios. We find that the SNRs for the memory modes decrease as mass ratio increases for $q \geq 10$. We complement this analysis by computing SNRs for the memory signals in the comparable mass ratio regime ($1 \leq q \leq 9$) using the `NRHybSur3dq8` model (red shaded

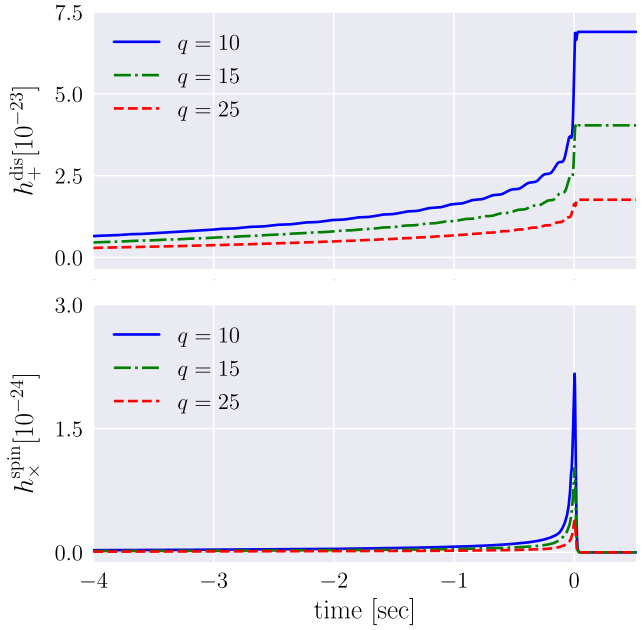

FIG. 15. Time evolution of the displacement memory $h^{\rm dis}(t)$ (upper panel) and spin memory $h^{\rm spin}(t)$ (lower panel) for BBHs with three different mass ratio q. Our system is a nonspinning BBH with total mass $M = 200M_\odot$, at a luminosity distance $D = 250$ Mpc and at an inclination $\iota = \pi/4$.

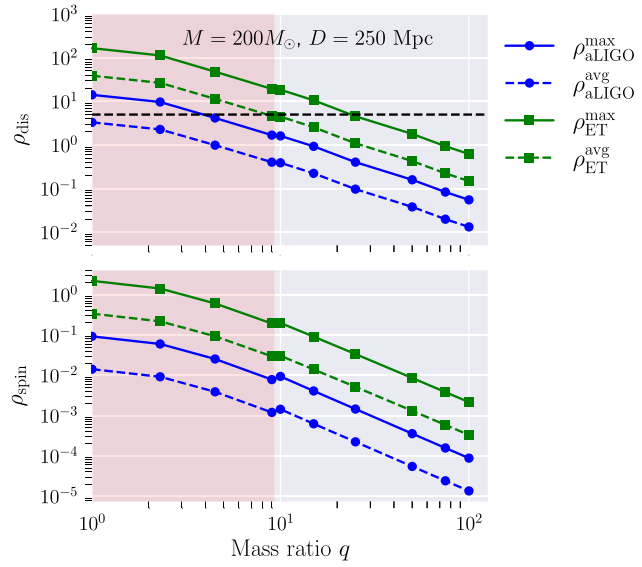

FIG. 16. Maximum SNR $\rho_{\rm max}$ (solid line) and angle-average SNR $\rho_{\rm avg}$ (dashed line) for the memory modes computed using the design sensitivity of the advanced LIGO (blue) and ET (green) as a function of the mass ratio q. We use $M = 200M_\odot$, $\chi = 0.0$, $e_{\rm ref} = 0.0$ and $D = 250$ Mpc. Both displacement and spin memory decreases as $\sim 1/q$. The shaded red region shows SNRs computed using the `NRHybSur3dq8` model over $1 \leq q \leq 9$ (details are in text). We note that SNRs for the displacement memory are likely overestimated due to the issue mentioned in footnote 3.

region). We confirm that the overall trend of SNR scaling ($\sim 1/q$) continues almost up to $q = 1$. Furthermore, we observe that the SNR values have a mostly smooth transition from the comparable mass regime (obtained using `NRHybSur3dq8` model) to intermediate mass ratio regime (obtained using α-scaled ppBHPT waveforms) providing further evidence on the robustness of the SNR computation in the $q \geq 10$ regime where waveform modeling is more challenging.

VI. DISCUSSION AND CONCLUSION

In this work, using a recently-developed spin [25] and higher multipole displacement memory model [12], we systematically investigate the total memory effects for intermediate mass ratio inspirals (IMRIs). Our work is motivated by binary systems formed through hierarchical mergers [37,38], for example, when a GW190521-like remnant captures a stellar-mass black hole. Such systems typically have a large total mass, large spin on the primary, and possibly residual eccentricity; features that potentially raise the prospect for memory detection especially when subdominant modes are included into the analysis.

To generate the oscillatory part of the IMRI waveform (which is used in the computation of memory), we use point particle black hole perturbation theory (ppBHPT) waveforms computed by solving the Teukolsky equation. The ppBHPT waveforms are then calibrated to NR simulations for $q \leq 10$ using a rescaling discussed in Sec. III. As IMRI waveform models are still under active development, we have furnished extensive comparisons (Figs. 2–5) between a hybrid EOB-NR surrogate `NRHybSur3dq8`, an aligned-spin effective one body model `SEOBNRv4HM`, and our calibrated ppBHPT waveforms. We find these models agree surprisingly well for the dominant contributions to the GW memory for mass ratios $q \leq 100$ despite being calibrated to NR simulations mostly in the comparable mass ratio regime. Section IV provides evidence that the results presented in our paper serve as a useful and reliable ballpark estimate of memory from IMRI binaries. We stress, however, that the agreement of the memory computation between models does not imply that the oscillatory waveforms themselves will necessarily agree, and building high-accuracy and extensive IMRI waveform models is an open and active area of work [74,98,99]. It will be important to repeat this study once these models become available.

To assess the detectability of the memory signal in current and future gravitational wave detectors (primarily considering Advanced LIGO and ET), we compute both the optimal and angle-averaged signal to noise ratios (SNRs) for different binary configurations. Specifically, we have explored the SNR's dependence on the total mass, mass ratio, spin of the primary black hole, and eccentricity using memory signals with and without including subdominant harmonic modes. We find that memory signals become

stronger when the primary black hole has positive spins, with the SNR growing by as much as a factor of 10 as the spin is varied from $\chi \leq 0$ to $\chi \approx 0.99$. Figure 12 shows that memory signals from nonspinning BBH systems far from the detectability threshold may be detected for spins near $\chi \approx 0.95$. We find that when mild to moderate eccentricity is introduced, memory signals show rich structures (see Figs. 13 and 14)—with additional modulations both in the displacement and spin memory. However, the memory signal's amplitude hardly changes due to eccentricity, and consequently the SNRs for the memory modes in different eccentric configurations remain largely unchanged (see Table II). We've also explored the SNR's dependence on mass ratio, largely confirming the overall expectation of that the memory signal (and hence SNR) will become weaker as the mass ratio increases. This follows from the fact that the oscillatory mode's amplitude decreases as $1/q$ in the large-mass-ratio limit. This trend is seen most clearly in Fig. 16 and continues almost up to equal-mass systems. One limitation of our study is that the displacement memory does not go to zero at late times, and we have not explored strategies for handling such signals. This poses a challenge for SNR computations that rely on Eq. (10), as a straightforward application of the Fourier transform will generate spurious high-frequency features that are known to overestimate the SNR. To overcome this issue, one can consider different tapering strategies [83,84] or alternative data analysis techniques (without tapering) that are specifically designed to handle these kinds of signals [85,86].

All of our main results have been obtained using the higher multipole displacement memory model [12] using an oscillatory waveform model with $(\ell, m) = (2,2)$, $(2,1), (3,3), (3,2), (3,1), (4,2), (4,3)$ modes in our computation. Unlike most previous works, our displacement memory results include contributions from higher-order modes that have been typically omitted in similar studies. We have therefore provided some comparisons to displacement memory effects computed with the (2,2) mode only. The inclusion of subdominant modes in the memory computation will "activate" modes such as the (3,1) memory mode, which (for nonspinning systems) we see from Fig. 2 has maximum power around $q \approx 2.5$. A representative sample of the mode hierarchy is shown in Figs. 9 and 10, which shows the orbital-plane symmetry obeyed by the (ℓ, m) and $(\ell, -m)$ oscillatory modes is also obeyed by the memory modes. We find that including subdominant modes has a small but non-negligible impact on the systems considered here. Table I directly compares SNR values with and without higher order modes finding a difference by about ~7% across different detectors.

Our results indicate that displacement memory effects in IMRIs could be detected in future generation detectors such as the Einstein Telescope. Detection in current generation detectors would, however, require some amount of luck (e.g. systems merging very close and/or with a large, positive spin on the primary) and/or combining many events to compute the evidence (similar to Ref. [26]). On the other hand, the spin memory would still be difficult to detect even for highly spinning, optimally oriented systems. As our SNR computations have been done assuming only one detector, repeating this study using a network of detectors would naively increase the memory SNRs by a factor of $\propto \sqrt{N_{\rm det}}$ where $N_{\rm det}$ is the number of GW detectors. However, a full study would be needed to include each detector's PSD, relative orientation factors that may suppress or enhance any particular detector's sensitivity to the incoming memory signal, and a more careful accounting of tapering effects.

Heavy binaries with large positive spins are particularly promising for memory detections. For hierarchical mergers with second-generation (or higher) component black holes, spins of up to $\chi \approx 0.9$ are expected [37,38,100–102]. The increased SNR at larger spin values would favorably contribute to forecasts for memory detection. However, to the best of our knowledge, all memory forecasts that have appeared in the literature (e.g. [20,26]) use population models that favor nonspinning systems similar to GW190514. We expect that future work on memory forecasts that include both subdominant modes and mixed population models (1g + 1g, 1g + 2g, etc.) may find more optimistic forecasts.

Finally, we note that in this work we have focused on IMRIs composed of a stellar origin BH and an IMBH. It is also possible to form IMRIs with the combination of an IMBH and a massive BH. Though their event rates are very uncertain, these are exciting and potentially very high SNR sources for the LISA detector [42]. Their high SNR should also make them good candidates for detecting GW memory.

ACKNOWLEDGMENTS

We thank Everett Gaige Field, Hamish Warburton, Collin Capano, and David Nichols for helpful discussions and interactions throughout this work, Colm Talbot for assistance with the PYTHON package GWMemory, Keefe Mitman for assistance with the SXS PYTHON package's memory module, and Alex Grant for assistance with a private PYTHON package that we refer to in this paper as GWForecasts. We further thank Colm, Keefe, and Alex for their help in facilitating a comparison documented in Appendix. We also thank an anonymous referee for raising important questions on an earlier version of our paper. A portion of this work was carried out while a subset of the authors were in residence at the Institute for Computational and Experimental Research in Mathematics (ICERM) in Providence, RI, during the Advances in Computational Relativity program. I. C. E. R. M. is supported by the National Science Foundation under Grant No. DMS-1439786. Simulations

were performed on CARNiE at the Center for Scientific Computing and Visualization Research (CSCVR) of UMassD, which is supported by the ONR/DURIP Grant No. N00014181255 and the MIT Lincoln Labs *SuperCloud* GPU supercomputer supported by the Massachusetts Green High Performance Computing Center (MGHPCC). This research was supported in part by the Heising-Simons Foundation, the Simons Foundation, and National Science Foundation Grant No. NSF PHY-1748958. The authors acknowledge support of NSF Grants No. PHY-2106755 (G. K.), No. PHY-1806665 and PHY-2110496 (T. I. and S. F.), and No. DMS-1912716 (T. I., S. F., and G. K.). T. I. acknowledges additional support from the Kavli Institute for Theoretical Physics, University of California, Santa Barbara through Kavli Graduate Fellowship. N. W. acknowledges support from a Royal Society–Science Foundation Ireland Research Fellowship. This publication has emanated from research conducted with the financial support of Science Foundation Ireland under Grant No. 16/RS-URF/3428.

APPENDIX: COMPARISON OF SXS, GWMemory, AND GWForecasts

Throughout this paper, we have performed numerical computations of the nonlinear displacement memory from oscillatory gravitational waveform modes. This direct computation, which is expected to be more accurate than analytic approximations, takes into account coupling between modes entering the energy flux expression (1).

Despite many appealing properties of a purely numerical memory computation, the associated software is sufficiently complicated that its helpful to have cross checks between independently written codes using different approaches. Throughout our paper, we have used the PYTHON package GWMemory [50], which is also a highly efficient code as it precomputes angular integrals appearing in Eq. (1). After the initial draft of our paper was completed, we became aware of two other codes that compute the displacement memory by a different means. One (currently nonpublic) code was recently used to compile forecasts (updating previous ones from Ref. [20]) for how long current and future detectors will need to operate in order to measure memory from binary black hole populations [83]. We will refer to this code as GWForecasts. A second code, a submodule of the SXS [103] PYTHON package, implements techniques developed in the paper *Adding Gravitational Memory to Waveform Catalogs using BMS Balance Laws* by Mitman *et al.* [104]. The SXS's memory submodule is designed to add memory to SXS waveform data obtained from the public catalog [51]. We wrote a wrapper around this submodule (implemented in GWTOOLS version 1.14) to allow users to generate memory when the waveform modes are instead represented as a PYTHON dictionary. This allows the memory to be easily computed as

```
import numpy as np
from gwmemory import time_domain_memory
as tdm
from gwtools import sxs_memory
import  gwforecasts.memories.displace-
ment as gwf
import gwsurrogate as gws

disp = gwf.DisplacementMemory(ell_max = 5)
model = gws.LoadSurrogate("NRHybSur3dq8")

chi = [0, 0, 0] # nonspinning BBH
t   = np.arange(-10000, 100, .1)

# mass ratio 8 system without spin
t, h, dyn = model(8, chi, chi, times=t,
f_low = 0)

h_mem, times      = tdm(h_lm = h, times = t)
h_mem_forecasts = disp. filter(h, t)
h_mem_sxs, times_sxs = sxs_memory(h, t)
```

In this appendix, we briefly compare memory computed with GWMemory (specifically, with a git commit hash of 2a4b8084144b13a3f542b1e132d9bc629d4ec9c1), SXS (specifically version 2022.4.3), and GWForecasts.

Figure 17 compares the SXS (solid red lines), GWMemory (dashed-dot black lines), and GWForecasts (dashed blue lines) computation for the displacement memory's (2,0) and (4,0) modes. The input waveform comes from the

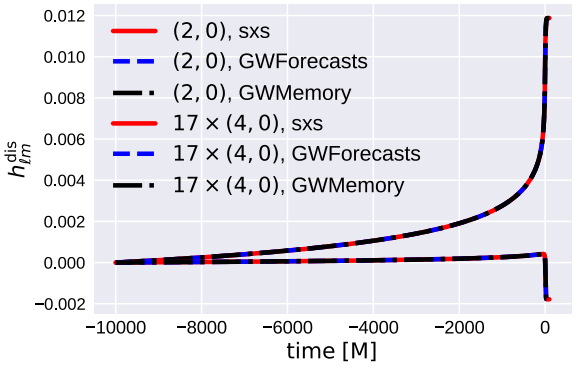

FIG. 17. Displacement memory modes for a nonspinning BBH with mass ratio $q = 8$ computed using the SXS (solid lines), GWForecasts (dashed lines), and GWMemory (dash-dot lines) packages. All available $\ell \leq 5$ oscillatory "input" modes are passed to these packages, which in turn perform a purely numerical computation of the memory. We find broad agreement between all three codes. Here we show the dominant (2,0) mode (whose final value is about 0.012) as well as the (4,0) mode, where we have multiplied the (4,0) mode's amplitude by 17 for visual assistance. Subdominant modes (not shown) are also in agreement.

NRHybSur3dq8 model for a $q = 8$, nonspinning BBH system. Both the (2,0) and (4,0) modes are visually identical among all three codes, as are many of the subdominant modes (not shown). In earlier versions of GWMemory (used to compile results from our paper's arXiv version 1) we noticed small differences in the (2,0) mode and sometimes large discrepancies in the subdominant modes.

[1] B. P. Abbott *et al.* (LIGO Scientific and Virgo Collaborations), GWTC-1: A Gravitational-Wave Transient Catalog of Compact Binary Mergers Observed by LIGO and Virgo during the First and Second Observing Runs, Phys. Rev. X **9**, 031040 (2019).

[2] R. Abbott, T. D. Abbott, S. Abraham, F. Acernese, K. Ackley, A. Adams, C. Adams, R. X. Adhikari, V. B. Adya, C. Affeldt *et al.*, GWTC-2: Compact Binary Coalescences Observed by LIGO and Virgo During the First Half of the Third Observing Run, Phys. Rev. X **11**, 021053 (2021).

[3] R. Abbott *et al.* (LIGO Scientific and Virgo Collaborations), Tests of general relativity with binary black holes from the second LIGO-Virgo gravitational-wave transient catalog, Phys. Rev. D **103**, 122002 (2021).

[4] Y. B. Zel'dovich and A. G. Polnarev, Radiation of gravitational waves by a cluster of superdense stars, Sov. Astron. **18**, 17 (1974), https://adsabs.harvard.edu/full/1974SvA....18...17Z.

[5] Vladimir B. Braginsky and Kip S. Thorne, Gravitational-wave bursts with memory and experimental prospects, Nature (London) **327**, 123 (1987).

[6] Demetrios Christodoulou, Nonlinear Nature of Gravitation and Gravitational-Wave Experiments, Phys. Rev. Lett. **67**, 1486 (1991).

[7] Luc Blanchet and Thibault Damour, Hereditary effects in gravitational radiation, Phys. Rev. D **46**, 4304 (1992).

[8] Ercan Kilicarslan and Bayram Tekin, Graviton mass and memory, Eur. Phys. J. C **79**, 114 (2019).

[9] Huan Yang and Denis Martynov, Testing Gravitational Memory Generation with Compact Binary Mergers, Phys. Rev. Lett. **121**, 071102 (2018).

[10] Sabrina Pasterski, Andrew Strominger, and Alexander Zhiboedov, New gravitational memories, J. High Energy Phys. 12 (2016) 053.

[11] David A. Nichols, Center-of-mass angular momentum and memory effect in asymptotically flat spacetimes, Phys. Rev. D **98**, 064032 (2018).

[12] Colm Talbot, Eric Thrane, Paul D. Lasky, and Fuhui Lin, Gravitational-wave memory: Waveforms and phenomenology, Phys. Rev. D **98**, 064031 (2018).

[13] Alan G. Wiseman and Clifford M. Will, Christodoulou's nonlinear gravitational wave memory: Evaluation in the quadrupole approximation, Phys. Rev. D **44**, R2945 (1991).

[14] D. Kennefick, Prospects for detecting the Christodoulou memory of gravitational waves from a coalescing compact binary and using it to measure neutron star radii, Phys. Rev. D **50**, 3587 (1994).

[15] Marc Favata, Nonlinear gravitational-wave memory from binary black hole mergers, Astrophys. J. Lett. **696**, L159 (2009).

[16] Marc Favata, Post-Newtonian corrections to the gravitational-wave memory for quasicircular, inspiralling compact binaries, Phys. Rev. D **80**, 024002 (2009).

[17] Marc Favata, The gravitational-wave memory effect, Classical Quantum Gravity **27**, 084036 (2010).

[18] Aaron D. Johnson, Shasvath J. Kapadia, Andrew Osborne, Alex Hixon, and Daniel Kennefick, Prospects of detecting the nonlinear gravitational wave memory, Phys. Rev. D **99**, 044045 (2019).

[19] Lior M. Burko and Gaurav Khanna, Climbing up the memory staircase: Equatorial zoom-whirl orbits, Phys. Rev. D **102**, 084035 (2020).

[20] Oliver M. Boersma, David A. Nichols, and Patricia Schmidt, Forecasts for detecting the gravitational-wave memory effect with Advanced LIGO and Virgo, Phys. Rev. D **101**, 083026 (2020).

[21] Marc Favata, Post-Newtonian corrections to the gravitational-wave memory for quasicircular, inspiralling compact binaries, Phys. Rev. D **80**, 024002 (2009).

[22] Keefe Mitman, Jordan Moxon, Mark A. Scheel, Saul A. Teukolsky, Michael Boyle, Nils Deppe, Lawrence E. Kidder, and William Throwe, Computation of displacement and spin gravitational memory in numerical relativity, Phys. Rev. D **102**, 104007 (2020).

[23] Lawrence E. Kidder, Scott E. Field, Francois Foucart, Erik Schnetter, Saul A. Teukolsky, Andy Bohn, Nils Deppe, Peter Diener, François Hébert, Jonas Lippuner *et al.*, SpECTRE: A task-based discontinuous galerkin code for relativistic astrophysics, J. Comput. Phys. **335**, 84 (2017).

[24] Jordan Moxon, Mark A. Scheel, and Saul A. Teukolsky, Improved cauchy-characteristic evolution system for high-precision numerical relativity waveforms, Phys. Rev. D **102**, 044052 (2020).

[25] David A. Nichols, Spin memory effect for compact binaries in the post-Newtonian approximation, Phys. Rev. D **95**, 084048 (2017).

[26] Paul D. Lasky, Eric Thrane, Yuri Levin, Jonathan Blackman, and Yanbei Chen, Detecting Gravitational-Wave Memory with LIGO: Implications of GW150914, Phys. Rev. Lett. **117**, 061102 (2016).

[27] Lucy O. McNeill, Eric Thrane, and Paul D. Lasky, Detecting Gravitational Wave Memory without Parent Signals, Phys. Rev. Lett. **118**, 181103 (2017).

[28] Moritz Hübner, Colm Talbot, Paul D. Lasky, and Eric Thrane, Measuring gravitational-wave memory in the first

LIGO/Virgo gravitational-wave transient catalog, Phys. Rev. D **101**, 023011 (2020).
[29] Neev Khera, Badri Krishnan, Abhay Ashtekar, and Tommaso De Lorenzo, Inferring the gravitational wave memory for binary coalescence events, Phys. Rev. D **103**, 044012 (2021).
[30] J. B. Wang *et al.*, Searching for gravitational wave memory bursts with the Parkes pulsar timing array, Mon. Not. R. Astron. Soc. **446**, 1657 (2015).
[31] B. P. Abbott *et al.* (LIGO Scientific and Virgo Collaborations), Observation of Gravitational Waves from a Binary Black Hole Merger, Phys. Rev. Lett. **116**, 061102 (2016).
[32] Moritz Hübner, Paul Lasky, and Eric Thrane, Memory remains undetected: Updates from the second LIGO/Virgo gravitational-wave transient catalog, Phys. Rev. D **104**, 023004 (2021).
[33] Hua Feng and Roberto Soria, Ultraluminous x-ray sources in the Chandra and XMM-Newton era, New Astron. Rev. **55**, 166 (2011).
[34] Dheeraj R. Pasham, Tod E. Strohmayer, and Richard F. Mushotzky, A 400 solar mass black hole in the ultraluminous x-ray source M82 X-1 accreting close to its Eddington limit, Nature (London) **513**, 74 (2014).
[35] Mar Mezcua, Observational evidence for intermediate-mass black holes, Int. J. Mod. Phys. D **26**, 1730021 (2017).
[36] R. Abbott *et al.* (LIGO Scientific and Virgo Collaborations), GW190521: A Binary Black Hole Merger with a Total Mass of $150M_{\odot}$, Phys. Rev. Lett. **125**, 101102 (2020).
[37] Zoheyr Doctor, Daniel Wysocki, Richard O'Shaughnessy, Daniel E Holz, and Ben Farr, Black hole coagulation: Modeling hierarchical mergers in black hole populations, Astrophys. J. **893**, 35 (2020).
[38] Davide Gerosa and Maya Fishbach, Hierarchical mergers of stellar-mass black holes and their gravitational-wave signatures, Nat. Astron. **5**, 749 (2021).
[39] Xiaolin Liu, Xiaokai He, and Zhoujian Cao, Accurate calculation of gravitational wave memory, Phys. Rev. D **103**, 043005 (2021).
[40] Nathan W. C. Leigh, Nora Lützgendorf, Aaron M. Geller, Thomas J. Maccarone, Craig Heinke, and Alberto Sesana, On the coexistence of stellar-mass and intermediate-mass black holes in globular clusters, Mon. Not. R. Astron. Soc. **444**, 29 (2014).
[41] Morgan MacLeod, Michele Trenti, and Enrico Ramirez-Ruiz, The close stellar companions to intermediate mass black holes, Astrophys. J. **819**, 70 (2016).
[42] Pau Amaro-Seoane, Jonathan R. Gair, Marc Freitag, M. Coleman Miller, Ilya Mandel, Curt J. Cutler, and Stanislav Babak, Astrophysics, detection and science applications of intermediate- and extreme mass-ratio inspirals, Classical Quantum Gravity **24**, R113 (2007).
[43] Christopher P. L. Berry, Scott A. Hughes, Carlos F. Sopuerta, Alvin J. K. Chua, Anna Heffernan, Kelly Holley-Bockelmann, Deyan P. Mihaylov, M. Coleman Miller, and Alberto Sesana, The unique potential of extreme mass-ratio inspirals for gravitational-wave astronomy, arXiv:1903.03686.
[44] Pau Amaro-Seoane, Detecting intermediate-mass ratio inspirals from the ground and space, Phys. Rev. D **98**, 063018 (2018).
[45] Pau Amaro-Seoane *et al.*, Laser interferometer space antenna, arXiv:1702.00786.
[46] Seiji Kawamura *et al.*, Current status of space gravitational wave antenna DECIGO and B-DECIGO, Prog. Theor. Exp. Phys. **2021**, 05A105 (2021).
[47] Manuel Arca Sedda *et al.*, The missing link in gravitational-wave astronomy: Discoveries waiting in the decihertz range, Classical Quantum Gravity **37**, 215011 (2020).
[48] Kip S. Thorne, Gravitational-wave bursts with memory: The Christodoulou effect, Phys. Rev. D **45**, 520 (1992).
[49] Marc Favata, The gravitational-wave memory from eccentric binaries, Phys. Rev. D **84**, 124013 (2011).
[50] GWMemory, https://github.com/ColmTalbot/gwmemory.
[51] Michael Boyle *et al.*, The SXS Collaboration catalog of binary black hole simulations, Classical Quantum Gravity **36**, 195006 (2019).
[52] James Healy and Carlos O. Lousto, Third RIT binary black hole simulations catalog, Phys. Rev. D **102**, 104018 (2020).
[53] Carlos O. Lousto and James Healy, Exploring the Small Mass Ratio Binary Black Hole Merger via Zeno's Dichotomy Approach, Phys. Rev. Lett. **125**, 191102 (2020).
[54] Nur E. M. Rifat, Scott E. Field, Gaurav Khanna, and Vijay Varma, Surrogate model for gravitational wave signals from comparable and large-mass-ratio black hole binaries, Phys. Rev. D **101**, 081502 (2020).
[55] Ryuichi Fujita and Hideyuki Tagoshi, New numerical methods to evaluate homogeneous solutions of the Teukolsky equation, Prog. Theor. Phys. **112**, 415 (2004).
[56] Ryuichi Fujita and Hideyuki Tagoshi, New numerical methods to evaluate homogeneous solutions of the Teukolsky equation. II:—Solutions of the continued fraction equation–, Prog. Theor. Phys. **113**, 1165 (2005).
[57] Shuhei Mano, Hisao Suzuki, and Eiichi Takasugi, Analytic solutions of the Teukolsky equation and their low frequency expansions, Prog. Theor. Phys. **95**, 1079 (1996).
[58] William Throwe, High precision calculation of generic extreme mass ratio inspirals, Ph.D. thesis, Massachusetts Institute of Technology, 2010.
[59] Black Hole Perturbation Toolkit, http://bhptoolkit.org/.
[60] Stephen O'Sullivan and Scott A. Hughes, Strong-field tidal distortions of rotating black holes: Formalism and results for circular, equatorial orbits, Phys. Rev. D **90**, 124039 (2014).
[61] Steve Drasco and Scott A. Hughes, Gravitational wave snapshots of generic extreme mass ratio inspirals, Phys. Rev. D **73**, 024027 (2006).
[62] Black Hole Perturbation Toolkit, http://bhptoolkit.org.
[63] Amos Ori and Kip S. Thorne, Transition from inspiral to plunge for a compact body in a circular equatorial orbit around a massive, spinning black hole, Phys. Rev. D **62**, 124022 (2000).
[64] Scott A. Hughes, Anuj Apte, Gaurav Khanna, and Halston Lim, Learning About Black Hole Binaries from

Their Ringdown Spectra, Phys. Rev. Lett. **123**, 161101 (2019).
[65] Pranesh A. Sundararajan, Gaurav Khanna, and Scott A. Hughes, Binary black hole merger gravitational waves and recoil in the large mass ratio limit, Phys. Rev. D **81**, 104009 (2010).
[66] Anuj Apte and Scott A. Hughes, Exciting black hole modes via misaligned coalescences: I. Inspiral, transition, and plunge trajectories using a generalized ori-thorne procedure, Phys. Rev. D **100**, 084031 (2019).
[67] Pranesh A. Sundararajan, Gaurav Khanna, and Scott A. Hughes, Towards adiabatic waveforms for inspiral into Kerr black holes. I. A new model of the source for the time domain perturbation equation, Phys. Rev. D **76**, 104005 (2007).
[68] Pranesh A. Sundararajan, Gaurav Khanna, Scott A. Hughes, and Steve Drasco, Towards adiabatic waveforms for inspiral into Kerr black holes: II. Dynamical sources and generic orbits, Phys. Rev. D **78**, 024022 (2008).
[69] Pranesh A. Sundararajan, Gaurav Khanna, and Scott A. Hughes, Binary black hole merger gravitational waves and recoil in the large mass ratio limit, Phys. Rev. D **81**, 104009 (2010).
[70] Anil Zenginoglu and Gaurav Khanna, Null Infinity Waveforms from Extreme-Mass-Ratio Inspirals in Kerr Spacetime, Phys. Rev. X **1**, 021017 (2011).
[71] Alexandre Le Tiec, Abdul H. Mroue, Leor Barack, Alessandra Buonanno, Harald P. Pfeiffer, Norichika Sago, and Andrea Taracchini, Periastron Advance in Black Hole Binaries, Phys. Rev. Lett. **107**, 141101 (2011).
[72] Maarten van de Meent and Harald P. Pfeiffer, Intermediate Mass-Ratio Black Hole Binaries: Applicability of Small Mass-Ratio Perturbation Theory, Phys. Rev. Lett. **125**, 181101 (2020).
[73] Niels Warburton, Adam Pound, Barry Wardell, Jeremy Miller, and Leanne Durkan, Gravitational-Wave Energy Flux for Compact Binaries Through Second Order in the Mass Ratio, Phys. Rev. Lett. **127**, 151102 (2021).
[74] Barry Wardell, Adam Pound, Niels Warburton, Jeremy Miller, Leanne Durkan, and Alexandre Le Tiec, Gravitational Waveforms for Compact Binaries from Second-Order Self-Force Theory, Phys. Rev. Lett. **130**, 241402 (2023).
[75] Kentaro Somiya (KAGRA Collaboration), Detector configuration of KAGRA: The Japanese cryogenic gravitational-wave detector, Classical Quantum Gravity **29**, 124007 (2012).
[76] R. Abbott, T. D. Abbott, F. Acernese, K. Ackley, C. Adams, N. Adhikari, R. X. Adhikari, V. B. Adya, C. Affeldt, D. Agarwal *et al.*, GWTC-3: Compact Binary Coalescences Observed by LIGO and Virgo During the Second Part of the Third Observing Run, arXiv:2111.03606 [Phys. Rev. X (to be published)].
[77] S. Hild *et al.*, Sensitivity studies for third-generation gravitational wave observatories, Classical Quantum Gravity **28**, 094013 (2011).
[78] Michele Maggiore, Chris Van Den Broeck, Nicola Bartolo, Enis Belgacem, Daniele Bertacca, Marie Anne Bizouard, Marica Branchesi, Sebastien Clesse, Stefano Foffa, Juan García-Bellido *et al.*, Science case for the Einstein telescope, J. Cosmol. Astropart. Phys. 03 (2020) 050.
[79] Benjamin P. Abbott *et al.* (LIGO Scientific Collaboration), Exploring the sensitivity of next generation gravitational wave detectors, Classical Quantum Gravity **34**, 044001 (2017).
[80] Evan D. Hall, Kevin Kuns, Joshua R. Smith, Yuntao Bai, Christopher Wipf, Sebastien Biscans, Rana X. Adhikari, Koji Arai, Stefan Ballmer, Lisa Barsotti *et al.*, Gravitational-wave physics with cosmic explorer: Limits to low-frequency sensitivity, Phys. Rev. D **103**, 122004 (2021).
[81] Evan D. Hall, Kevin Kuns, Joshua R. Smith, Yuntao Bai, Christopher Wipf, Sebastien Biscans, Rana X. Adhikari, Koji Arai, Stefan Ballmer, Lisa Barsotti *et al.*, Gravitational-wave physics with cosmic explorer: Limits to low-frequency sensitivity, Phys. Rev. D **103**, 122004 (2021).
[82] D. J. A. McKechan, C. Robinson, and B. S. Sathyaprakash, A tapering window for time-domain templates and simulated signals in the detection of gravitational waves from coalescing compact binaries, Classical Quantum Gravity **27**, 084020 (2010).
[83] Alexander M. Grant and David A. Nichols, Outlook for detecting the gravitational wave displacement and spin memory effects with current and future gravitational wave detectors, Phys. Rev. D **107**, 064056 (2023).
[84] Silvia Gasparotto, Rodrigo Vicente, Diego Blas, Alexander C. Jenkins, and Enrico Barausse, Can gravitational-wave memory help constrain binary black-hole parameters? A LISA case study, Phys. Rev. D **107**, 124033 (2023).
[85] Julian Westerweck, Yotam Sherf, Collin D. Capano, and Ram Brustein, Sub-atomic constraints on the Kerr geometry of GW150914, arXiv:2108.08823.
[86] Collin D. Capano, Miriam Cabero, Julian Westerweck, Jahed Abedi, Shilpa Kastha, Alexander H. Nitz, Alex B. Nielsen, and Badri Krishnan, Observation of a multimode quasinormal spectrum from a perturbed black hole, arXiv:2105.05238.
[87] Vijay Varma, Scott E. Field, Mark A. Scheel, Jonathan Blackman, Lawrence E. Kidder, and Harald P. Pfeiffer, Surrogate model of hybridized numerical relativity binary black hole waveforms, Phys. Rev. D **99**, 064045 (2019).
[88] T. Islam, S. E. Field, S. A. Hughes, G. Khanna, V. Varma, M. Giesler, M. A. Scheel, L. E. Kidder, and H. P. Pfeiffer, Surrogate model for gravitational wave signals from nonspinning, comparable-to large-mass-ratio black hole binaries built on black hole perturbation theory waveforms calibrated to numerical relativity, Phys. Rev. D **106**, 104025 (2022).
[89] Roberto Cotesta, Alessandra Buonanno, Alejandro Bohé, Andrea Taracchini, Ian Hinder, and Serguei Ossokine, Enriching the symphony of gravitational waves from binary black holes by tuning higher harmonics, Phys. Rev. D **98**, 084028 (2018).
[90] R. Abbott *et al.* (LIGO Scientific and Virgo Collaborations), GW190814: Gravitational waves from the coalescence of a 23 solar mass black hole with a 2.6 solar mass compact object, Astrophys. J. Lett. **896**, L44 (2020).
[91] Barak Zackay, Tejaswi Venumadhav, Liang Dai, Javier Roulet, and Matias Zaldarriaga, Highly spinning and

aligned binary black hole merger in the Advanced LIGO first observing run, Phys. Rev. D **100**, 023007 (2019).
[92] Ying Qin, Pablo Marchant, Tassos Fragos, Georges Meynet, and Vicky Kalogera, On the origin of black-hole spin in high-mass x-ray binaries, Astrophys. J. Lett. **870**, L18 (2019).
[93] Carl L. Rodriguez, Pau Amaro-Seoane, Sourav Chatterjee, and Frederic A. Rasio, Post-Newtonian Dynamics in Dense Star Clusters: Highly-Eccentric, Highly-Spinning, and Repeated Binary Black Hole Mergers, Phys. Rev. Lett. **120**, 151101 (2018).
[94] Johan Samsing, Eccentric black hole mergers forming in globular clusters, Phys. Rev. D **97**, 103014 (2018).
[95] Michael Ebersold, Yannick Boetzel, Guillaume Faye, Chandra Kant Mishra, Bala R. Iyer, and Philippe Jetzer, Gravitational-wave amplitudes for compact binaries in eccentric orbits at the third post-Newtonian order: Memory contributions, Phys. Rev. D **100**, 084043 (2019).
[96] Thierry Mora and Clifford M. Will, Numerically generated quasiequilibrium orbits of black holes: Circular or eccentric?, Phys. Rev. D **66**, 101501 (2002).
[97] Tousif Islam, Vijay Varma, Jackie Lodman, Scott E. Field, Gaurav Khanna, Mark A. Scheel, Harald P. Pfeiffer, Davide Gerosa, and Lawrence E. Kidder, Eccentric binary black hole surrogate models for the gravitational waveform and remnant properties: Comparable mass, nonspinning case, Phys. Rev. D **103**, 064022 (2021).
[98] Nicole Rosato, James Healy, and Carlos O. Lousto, Adapted gauge to small mass ratio binary black hole evolutions, Phys. Rev. D **103**, 104068 (2021).
[99] Alessandro Nagar, James Healy, Carlos O. Lousto, Sebastiano Bernuzzi, and Angelica Albertini, Numerical-relativity validation of effective-one-body waveforms in the intermediate-mass-ratio regime, Phys. Rev. D **105**, 124061 (2022).
[100] Davide Gerosa and Emanuele Berti, Are merging black holes born from stellar collapse or previous mergers?, Phys. Rev. D **95**, 124046 (2017).
[101] Maya Fishbach, Daniel E. Holz, and Ben Farr, Are LIGO's black holes made from smaller black holes?, Astrophys. J. Lett. **840**, L24 (2017).
[102] Emanuele Berti and Marta Volonteri, Cosmological black hole spin evolution by mergers and accretion, Astrophys. J. **684**, 822 (2008).
[103] SXS package, https://github.com/sxs-collaboration/sxs.
[104] Keefe Mitman, Dante A. B. Iozzo, Neev Khera, Michael Boyle, Tommaso De Lorenzo, Nils Deppe, Lawrence E. Kidder, Jordan Moxon, Harald P. Pfeiffer, Mark A. Scheel *et al.*, Adding gravitational memory to waveform catalogs using BMS balance laws, Phys. Rev. D **103**, 024031 (2021).